



University of Naples "Parthenope"
Department of Science and Technology

Ph.D. in Applied Sciences on Sea, Environment and Territory
XXIX Cycle

PERSEO (Piattaforma Embedded per la Ricerca del Sentiero di atterraggio ed Ostacoli)
Embedded Platform for UAS Landing Path and Obstacles Detection.

Ph.D. Student: Eng. Umberto Papa
Tutor: Prof. Eng. Giuseppe Del Core
Ph.D. Coordinator: Prof. Enrico Zambianchi

Dedication

Non sono bravo con le parole, ma la cosa che mi riesce sicuramente meglio è mostrare e trasmettere giorno per giorno la mia immensa passione per il volo a tutte le persone che mi circondano. Solo chi ama questa realtà sa cosa si prova ascoltare un motore di un aereo cento volte al giorno, ed alzare verso l'alto la testa cento volte. Questo percorso di dottorato, questo percorso di vita, non ha fatto altro che confermare la mia forte passione per il volo, dandomi l'opportunità di conoscere nuove cose e soprattutto nuove persone.

Le continue sfide createsi hanno fatto sì che mettessi in gioco me stesso e le mie idee, talvolta uscendo come perdente, ma spesso come vincitore.

A corredo di tutto, dietro le quinte, a mio sostegno c'è stata sempre la stessa squadra, quella vincente, la Famiglia.

Il sostegno costante mostrato da loro, mamma e papà, non ha fatto altro che fomentare la mia forte motivazione a farli sentire sempre più fieri di me, che per loro sarò sempre un batuffolo da 3 chili e mezzo piagnucolone. Grazie.

Poi c'è il gruppo *tuttapposto* (mia moglie, mia sorella e mio cognato), una parola che racchiude uno stile di vita, quello di non fermarsi mai al primo ostacolo, e soprattutto di rialzarsi dopo esser caduti e dire sempre *tuttapposto*. Grazie.

Spero con tutto il cuore di ritrovarmi tra vent'anni ed esser ancora affascinato, entusiasmato e motivato da questi mezzi che senza fili, senza un burattinaio dall'alto, sono in grado di librarsi in volo.

Fai quello che vuoi, fai quello che ti piace, sfida tutto e tutti e quando tutto va storto, ricorda che è sempre *tuttapposto*. Valeria *docet*.

Prizes and Awards

This Phd thesis topic was one of the winners of the Finmeccanica Young Innovation Contest 2015. The ceremony was held in the Universal Exposition in Milan, EXPO 2015.

2nd Place, Phd Category, Topic: Autonomous Systems

Project PERSEO (Piattaforma Embedded per la Ricerca Sentiero di Atterraggio ed Ostacoli)



Prize giving, from left with Mauro Moretti (Leonardo – Finmeccanica CEO), Stefania Giannini (Minister of Education), Gianni De Gennaro (Leonardo – Finmeccanica President) and Umberto Papa.

IEEE Student Highlights

This Phd thesis is an IEEE Aerospace and Electronic Systems Magazine Students Highlights.

U. Papa, (2017). Embedded Platform for Obstacle and Landing Path Detection – PERSEO.



Contents

<i>Dedication</i>	i
<i>Prizes and Awards</i>	ii
<i>IEEE Student Highlights</i>	iii
List of Figures	vi
List of Tables.....	x
1. Introduction to Unmanned Aircraft Systems (UASs).....	1
1.1 Introduction	1
1.2 Why UAS?	3
1.3 UASs Classification	4
2. Sonar Sensor Model for Safe Landing	12
2.1 Introduction	12
2.2 System design.....	13
2.3 Landing Plane Extraction	16
2.4 System Structure.....	17
2.5 Test Case and Results.....	20
3. Atmosphere effects on the SRS	27
3.1 Introduction	27
3.2 Theoretical Framework	27
3.3 SRSs Testing	29
3.4 Experimental analysis setup and Results.....	31
3.5 SRSs sensibility	38
3.6 DHT11 Temperature and Humidity Sensor	39
4. Integration among Ultrasonic and Infrared Sensors	42
4.1 Introduction	42
4.2 Infrared Sensor – IRS	42
4.3 Sensors data distance integration.....	50
4.4 Simulation and Results.....	53
5. UAS safe landing using an optical sensor and the space resection method	59
5.1 Introduction	59
5.2 Vision-based embedded system	60
5.2.1 Camera.....	60

5.2.2	Landing System Design	61
5.3	Camera position and attitude extraction.....	64
5.4	Camera Calibration	65
5.5	Points Extraction	68
5.6	Orientation	70
5.7	Validation procedure.....	71
5.8	Comparison and Results.....	73
5.9	Conclusions	76
6.	UAS Endurance Enhancement.....	77
6.1	Introduction.....	77
6.2	HUAS Conceptual Design	78
6.3	Weights Estimation and balloon sizing.....	81
6.4	Take-off Weight Estimation.....	81
6.5	Balloon Static Performance and Sizing.....	82
6.6	Preliminary Results	88
6.7	Conclusions	90
7.	Conclusions.....	93
8.	Appendix A.....	94
	UAVs Features.....	94
8.1	Conrad 450 ArF	94
8.2	RC EYE NovaX 350.....	95
8.3	RC EYE One Xtreme	97
	References.....	99

List of Figures

Figure 1.1. US Government funds for R&D in UASs/VTOLs - year 2000.	2
Figure 1.2. Worldwide VTOL manufacturing.....	2
Figure 1.3. Percentage of VTOL models produced over the world.	3
Figure 1.4. Leonardo da Vinci aerial screw, the first UAS in the history.	4
Figure 1.5. HALE and MALE air vehicles (data from Wikipedia).....	6
Figure 1.6. The MQ-1 Predator built by General Atomics Aeronautical Systems Inc.....	7
Figure 1.7. The RQ-4 A/B Global Hawk designed by Northrop Grumman.	7
Figure 1.8.Sky-Y built by Alenia Aermacchi (now Leonardo Company - Aircraft Division).....	8
Figure 1.9. The RQ-7A/B Shadow 200 manufactured by AAI.....	8
Figure 1.10. Possible quad-rotor configurations.	10
Figure 1.11. Conrad 450 (ArF) 35 MHz.....	10
Figure 1.12. RC Logger NovaX 350 ArF.....	11
Figure 1.13. RC Eye One Xtreme.	11
Figure 2.1. Model structure concept.....	13
Figure 2.2. HC-SR04 Ultrasonic Sensor Module front and back view details.....	13
Figure 2.3. Sequence Chart.	14
Figure 2.4. Arduino Mega 2560 micro controller (Arduino.cc, 2016).....	15
Figure 2.5. Arduino Wireless and SD shield, together used respectively for a wireless communication and for data storing.....	15
Figure 2.6. Electrical wiring scheme between SRSs and Arduino Uno. The scheme was made with Fritzing Software.....	16
Figure 2.7. CAD model of the SRSs holder, ABS printed in a cross configuration, where each position contain one SRS.	17
Figure 2.8. Whole SRSs system rendering, built thanks to a CAD software. In this figure were depicted the previous ABS SRSs holder and the electronic devices (Arduino, LCD display and battery).	18
Figure 2.9. SRS holder during 3D printing with the 3DRAG printer in the Laboratory of Air Navigation of the University of Naples “Parthenope”, Napoli, Italy.	18
Figure 2.10. Real SRSs system, including the wiring. In this case the wireless shield and the SD shield were in two different shields and not in the configuration of Figure 2.5.....	19
Figure 2.11. SD card shield used for SRSs data storing.....	19

Figure 2.12. SRSs system mounted below Conrad 350 ArF, used during preliminary tests.	20
Figure 2.13. System setup for the static sessions in the Flight Dynamic Laboratory.	20
Figure 2.14. Four SR04 distances from serial port (COM8).....	21
Figure 2.15. Data collection of distances from 20 to 150 cm, with SRS HC-SR04.	23
Figure 2.16. Landing Plane extrapolation trough the four SR04 distances.....	24
Figure 2.17. HC-SR04 rotary configuration.	24
Figure 2.18. Obstacle detected in the scanned area.....	25
Figure 2.19. Landing field mapping, obstacle detected.	25
Figure 2.20. Ultrasonic Radar window developed in Processing IDE.	25
Figure 3.1. a) HC-SR04, b) Parallax PING))).....	29
Figure 3.2. Concept of the structure.....	30
Figure 3.3. Detail: HC-SR04 and Arduino on the wood arm.....	30
Figure 3.4. KK-105 CH Climate Chamber used in this work.	31
Figure 3.5. Leica DISTO™ D3.....	32
Figure 3.6. HD2817T , transmitter, indicator, ON/OFF regulator, temperature and humidity datalogger.....	32
Figure 3.7. Virtual Instrument in LabVIEW™ window (National Instrument, 2003).....	33
Figure 3.8. Data changing for PING))) Parallax.	34
Figure 3.9. Data changing for HC-SR04.....	34
Figure 3.10. Scale factor and bias (RH = 10% - PING).....	35
Figure 3.11. Linear function for correction (RH = 10% - PING).	35
Figure 3.12. Scale factor and bias (RH = 10% - HC-SR04).	36
Figure 3.13. Linear function for correction (RH = 10% - HCSR04).	36
Figure 3.14. Scale factor and bias (T = 10 °C - PING).....	36
Figure 3.15. Linear function for correction (T = 10 °C - PING).....	37
Figure 3.16. Scale factor and bias (T = 10 °C - HC-SR04).....	37
Figure 3.17. Linear equation for correction (T = 10 °C - HC-SR04).....	37
Figure 3.18. PING))) distance acquisition.	39
Figure 3.19. HC-SR04 distance acquisition.	39
Figure 3.20. Sensor and Humidity sensor DHT11 (pin detail).	40
Figure 3.21. DHT11/Arduino Uno (Rev3) electric wiring scheme.....	40
Figure 4.1. IRS Sharp.....	42
Figure 4.2. IRS voltage acquisition during data collection, considering a range of distances 20-150 cm.....	43
Figure 4.3. Experimental Data collection, (Voltage vs. reciprocal Distance).....	44

Figure 4.4. Voltage vs. time IRS distance acquisition. Single acquisition time was 6 min (360 sec) @ 1 Hz.	46
Figure 4.5. Distance vs. time, IRS acquisition. Single acquisition time was 6 min (360 sec) @ 1 Hz.	48
Figure 4.6. IRS and SRS testing during a turn right maneuver.	49
Figure 4.7. IRS distances and extracted plane during Turn-right.	49
Figure 4.8. IRS acquisitions, UAS at 110 cm from the fixed surface (ground).	50
Figure 4.9. IRS and SRS acquisition system and wiring with Fritzing software.	50
Figure 4.10. Block diagram for integration.	52
Figure 4.11. Measurements results for IRS.	53
Figure 4.12. Standard deviation and variance for IRS.	54
Figure 4.13. Measurement results for SRS (HC-SR04).	54
Figure 4.14. Standard Deviation and variance of SRS.	55
Figure 4.15. Mean of SRS, IRS and x estimated comparison (@ISA).	55
Figure 4.16. Standard Deviation and Variance comparison (@ISA).	56
Figure 4.17. Mean of SRS, IRS and x estimated comparison (@ISA+15).	57
Figure 4.18. Standard Deviation and Variance comparison (@ISA+15).	57
Figure 5.1. Raspberry Pi Camera Board, it works with all models of Raspberry Pi 1 and 2.	61
Figure 5.2. Raspberry Pi 2 mod. B.	61
Figure 5.3. CSI port connection between Raspberry and the Camera module.	61
Figure 5.4. On-board vision system scheme.	62
Figure 5.5. On board vision system.	62
Figure 5.6. Detail of camera module mounted onboard.	62
Figure 5.7. Basic Landing Pattern.	63
Figure 5.8. Target reconnaissance on pattern.	64
Figure 5.9. Circular ring-coded target useful for camera calibration.	66
Figure 5.10. Calibration frames.	67
Figure 5.11. The 3D camera positions during the calibration procedure.	68
Figure 5.12. Detected target in a frame.	68
Figure 5.13. Coloured target on landing test field.	69
Figure 5.14. Two reference systems: the object SR (XYZ) and the camera SR (x' , y' , z').	70
Figure 5.15. Camera network obtained.	73
Figure 5.16. Error differences between LSM and CHT.	75
Figure 6.1. Conrad 450 (ArF) 35 MHz.	77
Figure 6.2. HUAS preliminary concept.	79
Figure 6.3. HUAS CAD 2D.	79

Figure 6.4. LiPo batteries used during tests.	80
Figure 6.5. Balloon configurations.....	82
Figure 6.6. Nomogram for initial inflation.....	84
Figure 6.7. Initial inflation in operative flight condition.....	85
Figure 6.8. Nomogram for expected gross static lift.....	86
Figure 6.9. Nomogram for expected gross static lift ($T_{\text{air}}=299\text{ K}$, $T_{\text{He}}=322\text{ K}$).	86
Figure 6.10. Gross static lift vs. balloon diameter.	89
Figure 6.11. Gas weight vs. balloon diameter.....	89
Figure 6.12. Relationship among design parameters.	90
Figure 6.13. Latest HUAS configuration, with directional propellers.	91
Figure 6.14. Newest configuration for non-linearity reduction.	91
Figure 8.1. Photos of 450 ArF quad-rotor.....	95
Figure 8.2. RC NovaX 350.	96
Figure 8.3. RC EYE One Xtream.....	97
Figure 8.4. RC Eye One Xtreme main dimensions.....	97

List of Tables

Table 1.1. Extract of UAV categories defined by UVS (Unmanned Vehicle Systems Association) International. Figures in the category “mini UAV” depend on different countries.	5
Table 1.2. Categories of Systems based upon air vehicle types (Austin, 2010).	5
Table 1.3. UASs Classification according to the US Department of Defense (DoD).	7
Table 1.4. Comparison among different VTOL concepts and design issues (adapted from (Valavanis, 2008), see text for coefficient explanation).	9
Table 2.1. HC-SR04 Technical Chart (HC-SR04, 2010 & Ping Parallax, 2016).	14
Table 2.2. International Standard Atmosphere model, based on average conditions at mid latitudes, as determined by the ISO's TC 20/SC 6 technical committee. It has been revised from time to time since the middle of the 20th century (Graham, 2006).	21
Table 3.1. SRSs technical chart, according to (Ping Parallax, 2016 & HC-SR04, 2010).	30
Table 3.2. KK-105 CH Technical data (Climatic Chamber KK-105, 2016).	31
Table 3.3. Data values setup.	33
Table 3.4. SRSs comparison before and after the correction.	38
Table 4.1. IRS features (Sharp, 2006).	43
Table 4.2. Error comparison in ISA conditions.	56
Table 4.3. Error comparison @ISA + 15.	57
Table 5.1. Internal orientation parameters of raspberry camera module.	67
Table 5.2. Precision values about the camera position and camera attitude expressed in millimetres, after a BA procedure.	74
Table 5.3. Position and attitude after LSM procedure.	75
Table 6.1. Endurance for the LiPo batteries previously considered.	80
Table 6.2. Lift comparison considering various gases.	83
Table 6.3. PVC mechanical characteristics.	88
Table 6.4. Operating conditions.	88
Table 6.5. HUAS vs. UAS endurance.	90
Table 8.1. 450 ArF main dimensions (CONRAD, 2006).	95
Table 8.2. Activated sensors.	96

1. Introduction to Unmanned Aircraft Systems (UASs)

1.1 Introduction

Unmanned Aerial Vehicles (UAVs), also denominated Unmanned Aircraft Systems (UAS) by FAA (Federal Aviation Administration), have gained great attention for many applications in the scientific, civil and military sectors. An UAS can be defined just as simply as a system (Valavanis, 2008). The system comprises a number of sub-systems which include the aircraft, its payloads, the control station(s) (and, often, other remote stations – Ground Station GS), aircraft launch and recovery sub-systems where applicable, support sub-systems, communication sub-systems, transport sub-systems, etc.

It must also be considered as part of a local or global air transport/aviation environment with its rules, regulations and disciplines.

Due to their ability to perform dangerous, sensitive, environmentally critical or dull tasks in a cost effective manner and with increased maneuverability and survivability, UASs play an important role in various military and civil applications. The numerous military applications include reconnaissance, surveillance, battle damage assessment, and communication relays.

Possible civil applications for UAS include monitoring and surveillance of areas (urban traffic, coast guard patrol, border patrol, detection of illegal imports, archeological site prospection, etc.), climate research (weather forecast, river flow, etc.), agricultural studies, air composition and pollution studies, inspection of electrical power lines, monitoring gas or oil pipe lines, entertainment and TV, etc. Most civilian uses of UASs require the air vehicle to fly at speeds lower than 50 kts (70 km/h) and at low heights, and many applications need the ability of the aircraft to hover (for example, for power line inspection, subsurface geology, mineral resource analysis, or incident control by police and fire services) (Valavanis, 2008).

Historically, the first UAS was introduced during World War I (1914-1919), registering the long participation of the US military with this type of crafts (OSD, 2002). These early forms of UASs were discarded by political leaders and military experts mainly for their inability to change the battlefield. Only few people, even then, predicted their future potentials.

UASs were also used in Vietnam, in the Desert Storm Operation (1991) and in the conflict of the Balkan Peninsula in the early 1990's. During this period, consensus toward UASs increased.

As early as in 1997, the total income of the UAS global market reached \$2.27 billion dollars, a 9.5% increase over 1996.

The Figure 1-1 show the total year (2000) funding of the US DOD (OSD, 2001), for UAS and VTOL (Vertical Take Off and Landing) vehicle design.

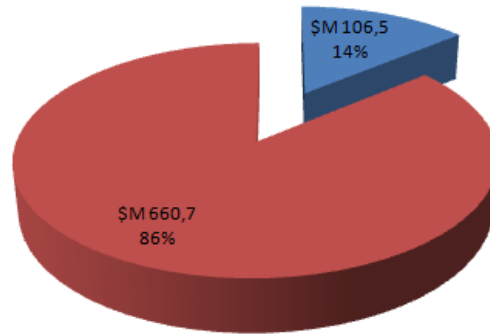


Figure 1-1. US Government funds for R&D in UASs/VTOLs - year 2000.

The events on 9/11, the war in Afghanistan and in Iraq have changed completely the perception about UASs putting them also on the everyday life map. Nowadays UASs are first subject in media coverage and TV documentaries. As stated in (Dickerson, 2007), Europe spend for UASs just about €2 billion, 13% of total US funds.

The VTOL vehicle segment is another evolving sector of the overall UAS market, as shown in Figure 1-2. Most of VTOLs were used for military application mainly in the US.

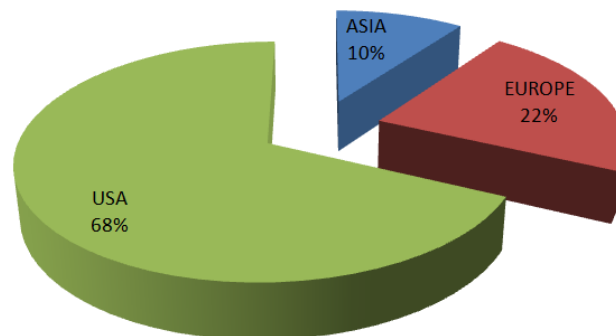


Figure 1-2. Worldwide VTOL manufacturing.

It is clear that unmanned aircrafts, fixed or rotary wing, have played a major role to the success of military operations (surveillance, search and rescue - SAR) but also in civilian applications the use of unmanned gained great consensus (traffic monitoring, search and rescue, TV entertainment, etc.).

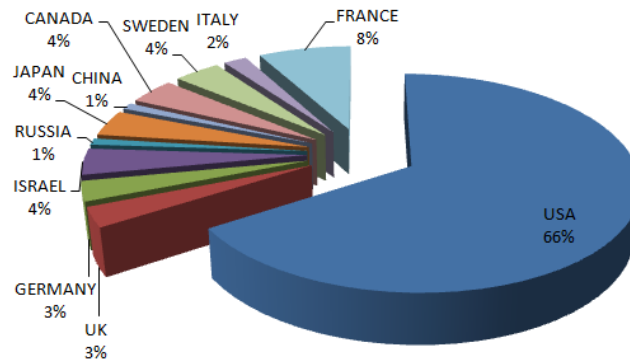


Figure 1-3. Percentage of VTOL models produced over the world.

The aim of this Ph.D. thesis is to classify and choose a type of UAS, and design an embedded sensors platform useful to assist the remote pilot during the landing procedure.

The design and implementation of an electronic platform were performed by using a bouquet of low cost sensors (ultrasonic, IR, Optics, etc.) for attitude control and obstacle-sense-and-avoid during the landing procedure at low altitude and low velocity.

Moreover, in some cases (e.g. urban traffic monitoring) this type of platform needs to execute extended missions with significant flight duration time. Increasing endurance generally comes at a cost in terms of fuel consumption and airframe complexity, resulting in reduced efficiency of payload and/or range for size, mass and financial cost. Chapter 6, at the end of this work, will explain a possible solution in order to increase the UAS endurance.

1.2 Why UAS?

As stated in (Valavanis, 2008; OSD 2002, 2005, Valavanis et al., 2008a, 2008b), UASs are preferred over manned aircraft mainly because the human cost of losing lives if the mission is unsuccessful is avoided, but also because unmanned vehicle have better and sustained alertness over humans during monotonous operations.

This is relevant in civilian applications, for example urban traffic, coast guard patrol, border patrol, detection of illegal imports, archeological site prospection, etc.), climate research (weather forecast, river flow, etc.), agricultural studies, air composition and pollution studies, inspection of electrical power lines, monitoring gas or oil pipe lines, entertainment and TV, etc. In this cases the advantages are justifying their preference over their manned counterparts.

The statement that UASs are best suited for “*dull, dirty and dangerous*” missions has merit and it is supported because:

- ✈ *Dull* - Long operations which require more than 30- or 40- hour missions are ideal for UASs involvement. This type of missions (in particular their duration), if manned, can compromise proficiency and functionality of crew members.
- ✈ *Dirty* - In case of chemically contaminated areas, the UASs alternative prevails. This solution will be fundamental for flying into nuclear clouds (as appended in Černobyl' disaster in April, 26th, 1986) avoiding humans usage.
- ✈ *Dangerous* – Operations like reconnaissance over enemy territory may result in loss of human lives, thus UASs are preferred.

1.3 UASs Classification

In modern times, UASs appeared during World War I (1914-1919). However the idea of a flying machine was conceived about 2500 years ago.

Autonomous mechanism and first aircrafts (flying machines) were studied and designed by Leonardo da Vinci (1452-1519), the first engineer. Da Vinci, in 1483 designed an aircraft that was able to hover, like today's helicopter do. This first aircraft was called aerial screw or air gyroscope (Figure 1-4).

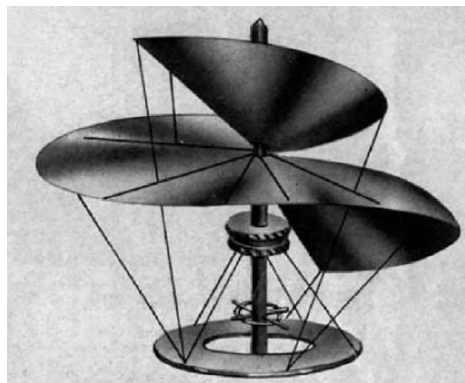


Figure 1-4. Leonardo da Vinci aerial screw, the first UAS in the history.

This machine is considered the ancestor of today's helicopters.

Currently, a broad range of UASs exists, from small and lightweight fixed-wing aircrafts to rotor helicopters, large-wingspan airplanes and quad-rotors, each one for a specific task, generally providing persistence beyond the capabilities of manned vehicles (Valavanis, 2008).

According to Table 1.1 (Eisenbess, 2004), UASs can be categorized with respect to mass, range, flight altitude and endurance.

Table 1.1. Extract of UAV categories defined by UVS (Unmanned Vehicle Systems Association) International. Figures in the category “mini UAV” depend on different countries.

Category Name	Mass [kg]	Range [km]	Flight Altitude [m]	Endurance [hours]
Micro	< 5	< 10	250	1
Mini	< 25/30/150	< 10	150/250/300	< 2
Close Range	25-250	10-30	3000	2-4
Medium Range	50-250	30-70	3000	3-6
High Altitude, Long Range	> 250	> 70	> 3000	> 6

This classification, based on radius of action in operation, has been replaced by newest terms (Austin, 2010), as follows:

- ✈ Long-range UAV – replaced by HALE and MALE;
- ✈ Medium-range UAV – replaced by TUAV;
- ✈ Close-range UAV – often referred to as MUAV or midi-UAV.

These new acronyms are explained in Table 1.2:

Table 1.2. Categories of Systems based upon air vehicle types (Austin, 2010).

Category	Range	Endurance [hr]
HALE – <i>High Altitude Long Endurance</i>	Altitude over 15 000 m	24+
MALE – <i>Medium Endurance Long Endurance</i>	Altitude 5 000 - 15 000 m	24
TUAV – <i>Medium Range or Tactical UAV</i>	Horizontal distance 100 – 300 km	
<i>Close-range UAV</i>	Horizontal distance about 100 km	
<i>MUAV or Mini UAV</i>	About 30 km and a weight below 20 kg	



Northrop Grumman – RQ-4 Global Hawk HALE

Length	13.5 m
Wingspan	35.4 m
Height	4.6 m
Empty weight	3850 kg
Max Take-off weight	10400 kg
Powerplant	1 x Turbofan Allison Rolls Royce AE3007H
Cruise Speed	575 km/h
Range	22779 km
Endurance	32+ hours
Service ceiling	60000 ft



General Atomics – RQ-1 Predator MALE

Length	8.22 m
Wingspan	14.8 m
Height	2.1 m
Wing Area	11.5 m ²
Empty Weight	512 kg
Max Take-off weight	
Powerplant	1 x Rotax 914F turbocharged four- cylinder engine
Cruise Speed	130 – 165 km/h
Range	1100 km
Endurance	24 hours
Service Ceiling	25000 ft

Figure 1-5. HALE and MALE air vehicles (data from Wikipedia).

The US Department of Defence (DoD) also has classified UASs into five categories as shown in Table 1.3 (US Army, 2010).

Table 1.3. UASs Classification according to the US Department of Defense (DoD).

Category	Size	Maximum Takeoff Weight [kg]	Normal Operating Altitude [m]	Airspeed [km/h]
Group 1	Small	0-9.9	< 365 AGL*	< 185.2
Group 2	Medium	10-24.9	< 1066.8	< 463
Group 3	Large	< 599	< 5486.4 MSL**	< 463
Group 4	Larger	> 599	< 5486.4 MSL	Any Airspeed
Group 5	Largest	> 599	> 5486.4	Any Airspeed

*AGL = Above Ground Level

**MSL = Mean Sea Level

Considering Table 1.1, some Large UASs in service were depicted in Figures 1.6 to 1.9.

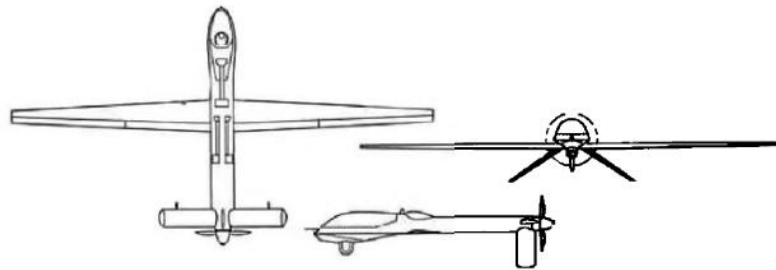


Figure 1-6. The MQ-1 Predator built by General Atomics Aeronautical Systems Inc.

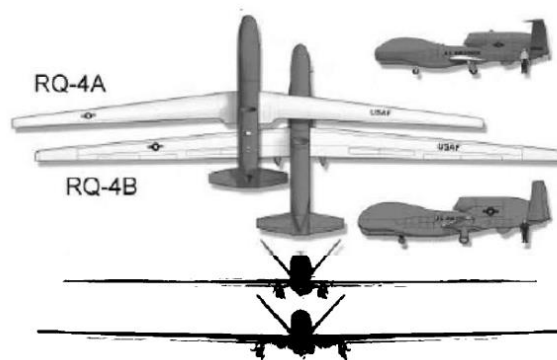


Figure 1-7. The RQ-4 A/B Global Hawk designed by Northrop Grumman.



Figure 1-8.Sky-Y built by Alenia Aermacchi (now Leonardo Company - Aircraft Division).

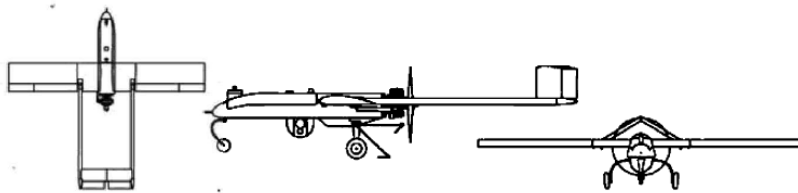


Figure 1-9. The RQ-7A/B Shadow 200 manufactured by AAI.

VTOL (Vertical Take-Off and Landing) aircrafts provide many advantages over Conventional Take-Off and Landing (CTOL) vehicles. Most notable are the capability of hovering in place and the small area required for take-off and landing.

Among VTOL aircrafts such as conventional helicopters and crafts with rotors like the tilt-rotor and fixed-wing aircrafts with directed jet thrust capability, the quad-copter, or quad-rotor (a helicopter with four rotors fixed on the ends of a cross-shaped frame), is very frequently chosen, especially in the academic research on mini or micro-size UAVs, as an effective alternative to the high cost and complexity of the conventional rotorcrafts, due to its ability to hover and move without the complex system of linkages and blade elements present in a standard single-rotor vehicle (Nonami et al., 2010, Ch. 1). Employing four rotors to create differential thrust, the quad-rotor gains flexibility, swift manoeuvrability and increased payload. A useful comparison of different types of VTOL miniature flying robots (MFR) can be found in (Nonami et al., 2010). Table 1.4, adapted from (Austin, 2010), gives quality indexes (from 1=bad, to 4=very good) for some design issues pertaining to different VTOL vehicle concepts, namely, bird-like (A), single-rotor (B), tandem rotors (C), insect-like (D), axial rotor (E), blimp (F), co-axial rotors (G), quad-rotor (H).

Table 1.4. Comparison among different VTOL concepts and design issues (adapted from (Valavanis, 2008), see text for coefficient explanation).

Design driver	A	B	C	D	E	F	G	H
Mechanics simplicity	1	1	1	1	3	4	3	4
Aerodynamics complexity	1	1	1	1	1	3	1	4
Low-speed flight	2	4	3	2	3	4	4	4
Stationary flight	1	4	4	2	4	3	4	4
Control cost	2	1	2	1	1	3	4	3
Payload/volume	2	2	3	1	2	1	4	3
Maneuverability	3	4	3	3	2	1	2	3
High-speed flight	3	2	2	3	4	1	1	3
Miniaturization	2	2	2	4	3	1	4	3
Power cost	3	2	2	3	2	4	2	1
Survivability/Endurance	2	1	1	3	3	3	3	1
Total quality index	22	24	24	24	28	28	32	33

The quad-rotor has a good ranking among VTOL vehicles, yet it has some drawbacks. For example, the craft size is comparatively larger, energy consumption is greater, therefore providing short flight time, and the control algorithms are very complicated, due to the fact that only four actuators are used to control the six degrees of freedom (DOF) of the craft (a quad-rotor is a typical example of an under-actuated system). Moreover, the changing aerodynamic interference patterns between the rotors have to be taken into account (Austin, 2010; Chap. 3). Unlike planes, there is no rudder, no ailerons, just propellers, typically brushless. The only way to modulate flight is by spinning the rotors at different speeds.

Light UASs quad-rotors use plastic propellers, which resist breaking on impact because they are flexible and safer. Some models use carbon fiber or other more rigid materials (planes frequently use wood or nylon/glass). Carbon fiber propellers are dangerous, even deadly, and should be used only by experienced pilots and well away from people. Unless extreme performance is a concern, the benefits of carbon fiber over plastic are marginal on multi-rotors. For this type of UASs the clockwise/counterclockwise pairing of every two motors is important. In Figure 1-10 are depicted some arrangements for a number of quad-rotor types.

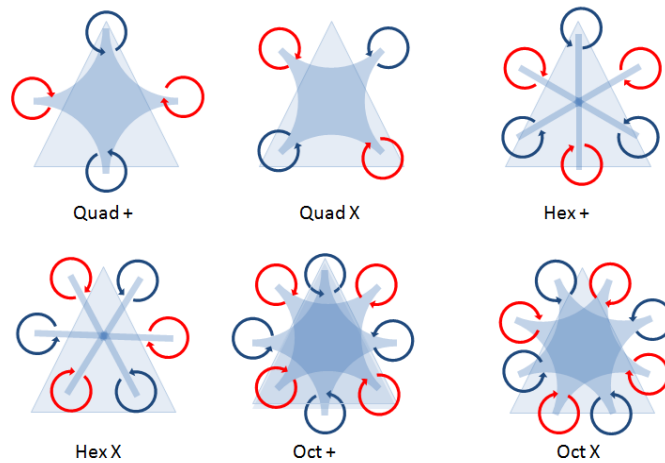


Figure 1-10. Possible quad-rotor configurations.

The UAS heading is represented by the top vertex of blue triangle (Figure 1-10), and the circular symbols represent the clockwise (red) and counter clockwise (blue) of the propellers' rotation.

This work proposes to design and improve a safe landing system of a non-expensive, commercial quad-rotor, by applying a series of low-cost sensors, for obstacle detection and attitude check during landing. The mini quad-rotors chosen are: Conrad Quadrocopter 450 ARF (Figure 1-11), RC Eye NovaX 350 (ArF) (Figure 1-12) and RC Eye One Xtreme (Figure 1-13). The equipment will be composed by: a Global Positioning System (GPS) receiver module, an Inertial Measurement Unit (IMU), a sonar altimeter, IR sensors, a small camera module and main microcontroller hardware (Arduino, Raspberry). Typical endurance is less than 30 minutes (without any payload on board).



Figure 1-11. Conrad 450 (ArF) 35 MHz.



Figure 1-12. RC Logger NovaX 350 ArF.



Figure 1-13. RC Eye One Xtreme.

The work of this Ph.D. thesis was strongly related to the acquisition system and sensors design for navigation data. The flight control algorithms were not considered. The technical specifications of the UASs are reported in Appendix A.

The sensors considered in this work are:

- ✈ Ultrasonic Sensor (SRS) – Sonar Sensor Model for Safe Landing (Chapter 2) and Atmosphere Effects Correction (Chapter 3);
- ✈ Infrared Sensor (IRS)– Integration among Ultrasonic and Infrared Sensor (Chapter 4);
- ✈ Optical Sensor (OPS) – Safe Landing procedure through Raspberry Pi Camera using Space Resection (Chapter 5).

Chapter 6 describes a new concept of UAS, in order to increase its endurance during the flight. The last chapter (Chapter 7) draws conclusions and addresses further work on the investigated topics.

2. Sonar Sensor Model for Safe Landing

2.1 Introduction

In UASs (Unmanned Aerial Systems) applications, it is important to find and track all scenario properties (e.g. obstacles). Performing obstacles and terrain avoidance from an UAS platform is challenging for several reasons (Valanakis, 2007). The UAS limited payload and power available give significant limitations on the total size, weight and power requirements of potential sensors. Embedded sensors systems like LIDAR and RADAR are typically too large and heavy for the UAS.

The sonar sensor tracking is one of the best ways to detect any obstacle in a flight zone, like bats or dolphins do. In short, a signal time delay, measured from the ultrasonic echo pin, gives distance measurements considering the speed of sound. The fundamental approach is to calculate the distance from the delay of the ultrasonic burst.

In civilian applications, UASs are mostly used due to their low cost and size. The cost of these UASs partially depends on the embedded sensors used for the flight control (IMU, GNSS, etc.). However, in some conditions, such as urban or low altitude operations, the GNSS receiver antenna is prone to losing the line-of-sight from the satellite, therefore making the GNSS receiver unable to deliver high-quality position information. This is quite dangerous for closed-loop control systems during the landing. Therefore, in these cases an ultrasonic sensor (SRS – Sonar Ranging Sensor) may be very useful for altitude control. Moreover, SRSs require lower computational efforts to provide target distance than camera-based systems, and have higher energy efficiency than laser ones.

Furthermore, obstacle detection is an important task for fully autonomous UASs. Ultrasonic proximity sensors are a good compromise in terms of cost, energy efficiency and accuracy for low-distance obstacle detection and altitude control.

The goal of this chapter is to design and evaluate a SRSs system useful for assisting UASs during landing. The system should be able to detect any obstacles on the landing field. In the same time the system maps the ground, and if the tilt angle of the field is greater than 30 degrees, the landing procedure is aborted. The range of altitude considered is 20 – 150 cm from the ground (landing field).

2.2 System design

The overall system is composed by four ultrasonic sensor HC-SR04 (HC-SR04, 2010), one microcontroller Arduino Mega 2560 (Arduino.cc, 2016), cables and a standing structure. Figure 2-1 shows the system concept:

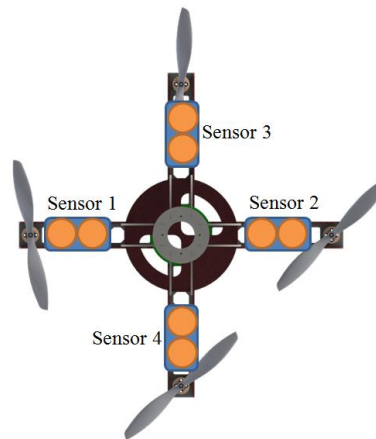


Figure 2-1. Model structure concept.

The ultrasonic sensor module HC-SR04 (Figure 2-2) provides a distance datum range of 2 - 400 cm no-contact measurement function, the range of accuracy can reach up to 3 mm. The module includes ultrasonic transmitters, receivers and control circuit. The shield has four pins (Vcc, Ground, Echo and Trigger).



Figure 2-2. HC-SR04 Ultrasonic Sensor Module front and back view details.

Table 2.1. HC-SR04 Technical Chart (HC-SR04, 2010 & Ping Parallax, 2016).

	HC-SR04	Parallax PING)))
Supply Voltage	5V DC	5V DC
Supply Current	15mA	30mA; 35mA max
Range	2-400 cm	2-300 cm
Input Trigger	10µs TTL pulse	2µs min, 5µs typ.
Echo pulse	Pos. TTL pulse	115µs to 18.5ms
Burst Frequency	40 kHz	40kHz for 200µs
Measuring Angle	<17° for side	<20° for side
Dimension	45x20x15mm	45.7x21.3x16mm

In order to make measurements with both ultrasonic sensors, the following procedures (HC-SR04, 2010) have been carried out (see Figure 2-3):

- ✦ Send a pulse signal of at least 10 µs (HLT – High Level Signal) on the trigger pin for HC-SR04;
- ✦ The ultrasonic transceiver automatically sends eight 40 kHz ultrasonic waves to the target and detect whether there is a pulse signal back;
- ✦ A pulse waveform is transmitted on Echo and IO pins. The pulse width is comparable with the time of fly.

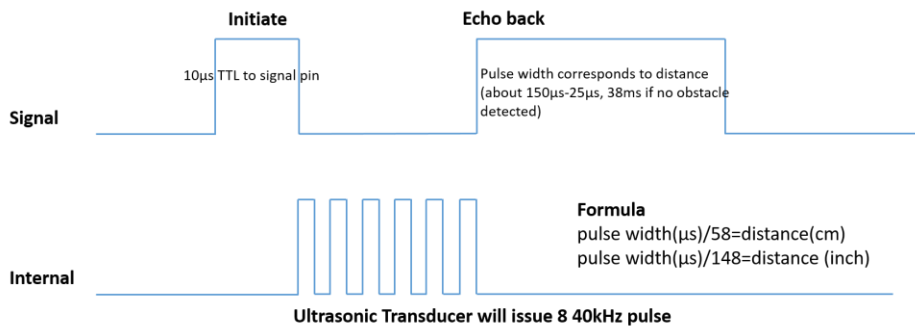


Figure 2-3. Sequence Chart.

The distance d was given by:

$$d = \frac{(HLT * a)}{2} \tag{2.1}$$

where HLT was high-level time and a is the speed of sound (340 m/s in the air at 20°C). If no obstacle is detected, the output pin will give a 38ms high-level signal.

Ultrasonic sensors work at 5V DC and they were linked to a microcontroller Arduino (Arduino.cc, 2010 & Timmins, 2011) through the four digital pins for HC-SR04.

The microcontroller platform was the single board Arduino Mega 2560 (Figure 2-4).



Figure 2-4. Arduino Mega 2560 micro controller (Arduino.cc, 2016).

The Arduino Mega 2560 Microcontroller is based on the ATmega2560. It has 54 digital input/output pins (of which 15 can be used as PWM outputs), 16 analog inputs, 4 UARTs (hardware serial ports), a 16-MHz crystal oscillator, a USB connection, a power jack, an ICSP header, and a reset button. It contains components needed to support the microcontroller; simply connect it to a computer with a USB cable or power it with an AC/DC adapter or battery to get started.

Arduino acquires data distances from ultrasonic sensors and sends them to a PC laptop, via USB interface. It is possible to perform this operation also via Wireless (Bluetooth or Wi-Fi), thanks to a specific module (Figure 2-5) added to Arduino board.

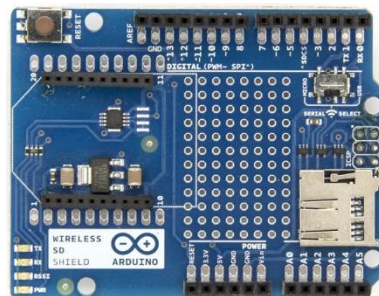


Figure 2-5. Arduino Wireless and SD shield, together used respectively for a wireless communication and for data storing.

The wiring between the SRS and Arduino was very simple, as depicted by the electrical scheme in the figure below:

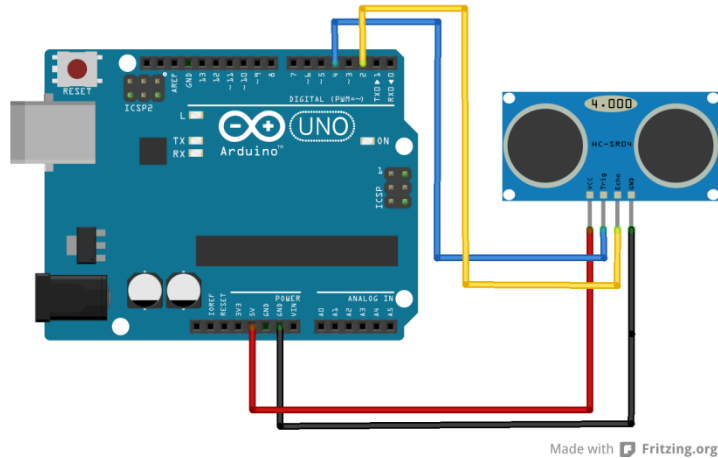


Figure 2-6. Electrical wiring scheme between SRSs and Arduino Uno. The scheme was made with Fritzing Software.

Figure 2-6 considers (as an example) the SRS coupled with an Arduino Uno, but the wiring remains the same also for Arduino Mega.

2.3 Landing Plane Extraction

The four sensors can extract distance measurements, useful for landing fields glide estimation. In general, a plane is described by an equation of the form $ax+by+cz+d=0$, just solving Equation (2.2) with the Laplace rule:

$$\begin{bmatrix} (x-x_1) & (y-y_1) & (z-z_1) \\ (x_2-x_1) & (y_2-y_1) & (z_2-z_1) \\ (x_3-x_1) & (y_3-y_1) & (z_3-z_1) \end{bmatrix} = 0 \quad (2.2)$$

So:

$$a(x-x_1)+b(y-y_1)+c(z-z_1)=0 \quad (2.3)$$

Where the coefficients a , b and c are:

$$a = \begin{bmatrix} (y_2-y_1) & (z_2-z_1) \\ (y_3-y_1) & (z_3-z_1) \end{bmatrix} \quad (2.4)$$

$$\mathbf{b} = \begin{bmatrix} (x_2 - x_1) & (z_2 - z_1) \\ (x_3 - x_1) & (z_3 - z_1) \end{bmatrix}$$

$$\mathbf{c} = \begin{bmatrix} (x_2 - x_1) & (y_2 - y_1) \\ (x_3 - x_1) & (y_3 - y_1) \end{bmatrix}$$

Remember that if $d=0$, the plane is positioned in the origin of the Cartesian coordinate system. The plane (landing field) can also be described by the "point and normal vector" (Equation 2.5). A suitable normal vector is given by the cross product:

$$\mathbf{n} = (\mathbf{p}_2 - \mathbf{p}_1) \times (\mathbf{p}_3 - \mathbf{p}_1) \quad (2.5)$$

and the point \mathbf{p}_0 can be taken to be any of the given points p_1 , p_2 or p_3 . In this work, the normal vector method has been utilized, where p_1 , p_2 and p_3 are points from ultrasonic sensors. If four ultrasonic sensors are considered, the points extracted are p_1 , p_2 , p_3 and p_4 respectively.

2.4 System Structure

For a compact and light structure, overall the components of the acquisition systems has been contained in an *ad-hoc* platform. In order to extract the four (or three) distance points, a cross configuration of the sensors has been chosen (Figure 2-7). The distance between sensors is the minimum, in order to eliminate interference among them.

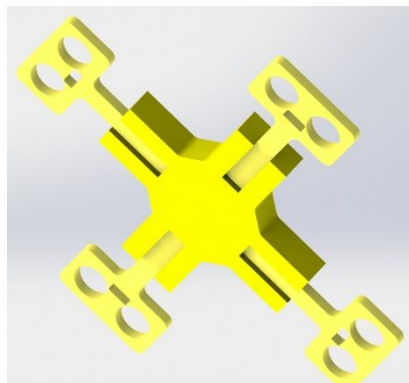


Figure 2-7. CAD model of the SRSs holder, ABS printed in a cross configuration, where each position contain one SRS.

The four ultrasonic sensors in a cross configuration, the microcontroller and the battery have been installed in the structure shown in Figure 2-8.

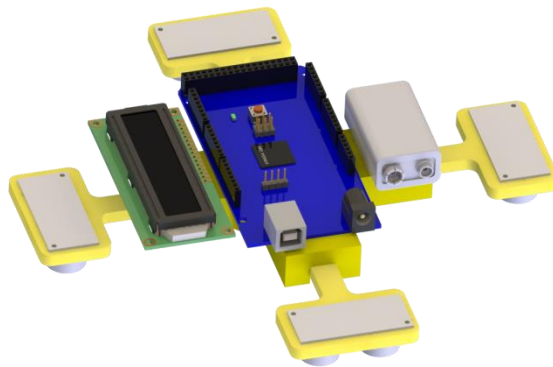


Figure 2-8. Whole SRSs system rendering, built thanks to a CAD software. In this figure were depicted the previous ABS SRSs holder and the electronic devices (Arduino, LCD display and battery).

The rendering in Figure 2-8 considers the material property and the real dimensions (scale 1:1) of the objects, in order to evaluate if there are interactions between them before the real installation.

The final structure has been realized thanks to a 3D printer, and for simplicity of manufacturing the whole structure was divided in various subcomponents. Figure 2-9 show the printing of the arm which contains the ultrasonic sensor.

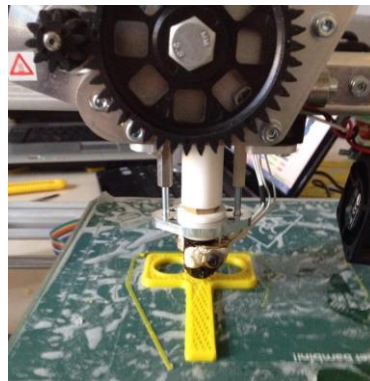


Figure 2-9. SRS holder during 3D printing with the 3DRAG printer in the Laboratory of Air Navigation of the University of Naples “Parthenope”, Napoli, Italy.

The material used for this cover structures was plastic ABS (Acrylonitrile Butadiene Styrene). They were printed out by a 3D printer (3DRAG, 2016) available in the Laboratory of Navigation. This hardware can print objects of maximum size of 20 x 20 x 20 cm using ABS or PLA (Polylactic acid or polylactide) 3 mm wires. The printer uses the X/Y for printing plane and Z for the cart; this particular configuration allows to simplify the extrusion system which no

longer have to move on a horizontal axis, is simply fixed to the structure that moves along the *Z axis* (3DRAG, 2016).

The complete system was depicted in figure below:

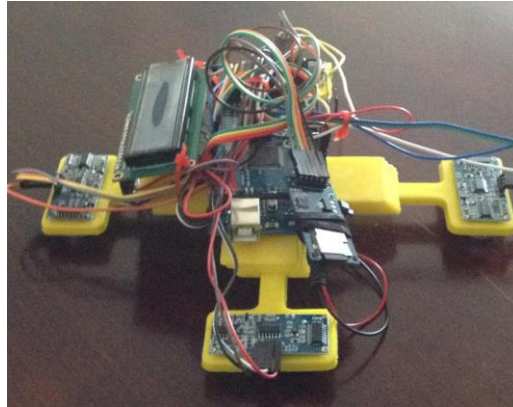


Figure 2-10. Real SRSs system, including the wiring. In this case the wireless shield and the SD shield were in two different shields and not in the configuration of Figure 2-5.

To get a feedback in real time of the standalone system, a LCD (16x2) display was mounted. Furthermore, a micro SD card shield (Figure 2-11) was installed in order to have the system data storing in case of wireless shield (Figure 2-5) fault. The overall system weight was about 250 gr.

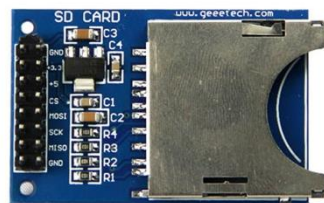


Figure 2-11. SD card shield used for SRSs data storing.

The system, on UAS mounted, is depicted in Figure 2.12:



Figure 2-12. SRSs system mounted below Conrad 350 ArF, used during preliminary tests.

2.5 Test Case and Results

For the experimental data collection, it was considered a distance range of 20 to 160 cm, a typical range covered during a small UAS landing procedure (Farid bin Misnan et. al., 2012). The system (cyan box in Figure 2-13) was initially tested in static sessions and positioned on a tripod.

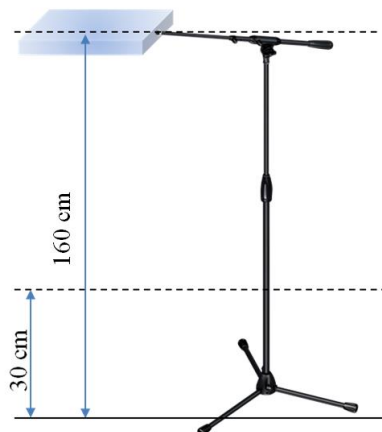


Figure 2-13. System setup for the static sessions in the Flight Dynamic Laboratory.

The distance extracted depends on the speed of sound, defined as follow:

$$a = \sqrt{\gamma RT} \quad (2.6)$$

Where γ is the adiabatic index, R is the molar gas constant (approximately 8.3145 J/mol·K) and T is the temperature (K). It is clear that the speed of sound depends on the transmission material (e.g. air, water, wall, etc.) and temperature. This aspect is dealt with in Chapter 3. In this case, the test was conducted in ISA (International Standard Atmosphere) conditions, see Table 2.2.

Table 2.2. International Standard Atmosphere model, based on average conditions at mid latitudes, as determined by the ISO's TC 20/SC 6 technical committee. It has been revised from time to time since the middle of the 20th century (Graham, 2006).

International Standard Atmosphere ICAO	
Temperature MSL*	15°C - 288.15 K
Pressure MSL*	101325 Pa
Density	1.225 Kg/m ³
Humidity	0%

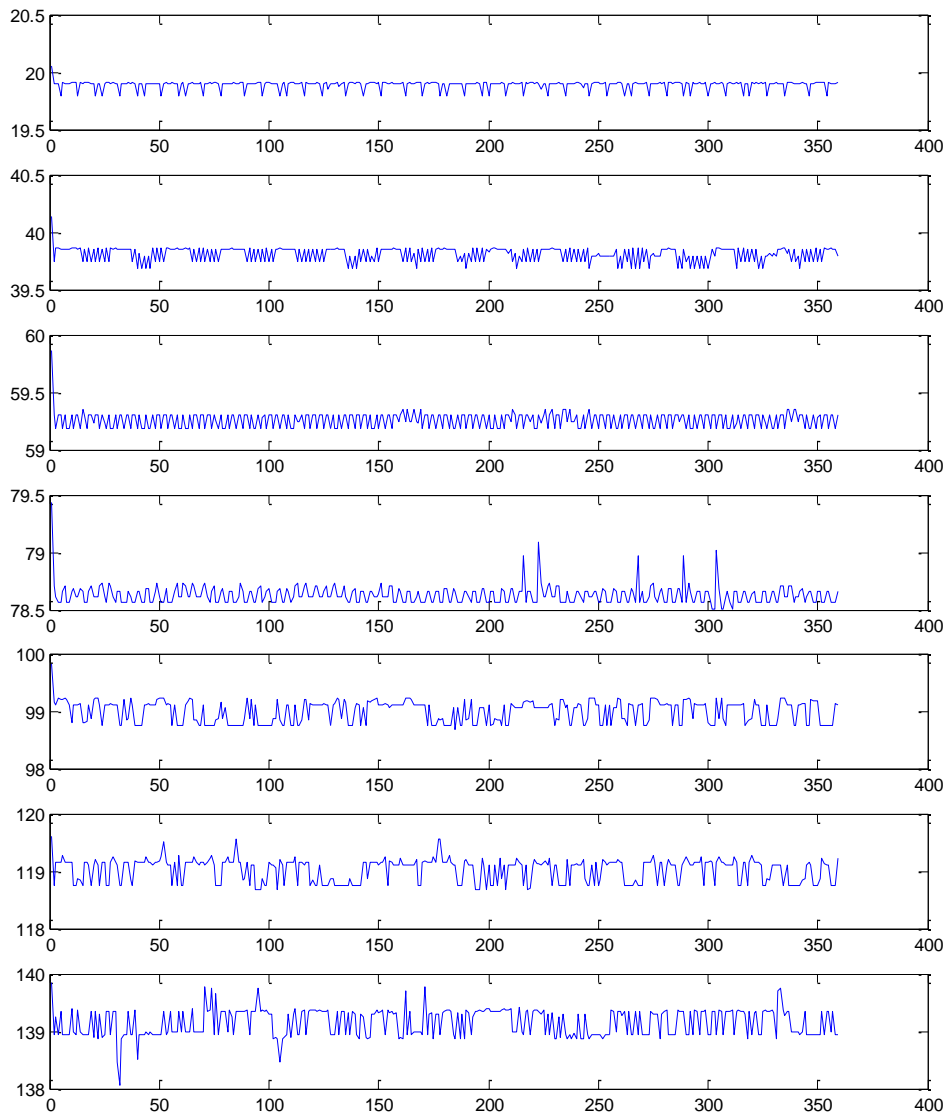
*MSL = Mean Sea Level

The data collected was useful to determinate the SR04 performance, in terms of mean, standard deviation and variance. Preliminary results of data distances, acquired from COM8 port (Figure 2-14) and computed in Matlab®, were shown below:

98	103	108	102
99	104	106	102
98	103	106	102
97	103	107	102
97	109	108	102
98	104	105	103
98	105	104	102
98	104	102	103
98	103	105	102
97	103	105	201
97	102	104	103
96	106	108	102
97	105	103	101
96	106	106	102

Figure 2-14. Four SR04 distances from serial port (COM8).

The data results confirm that accuracy of the ultrasonic sensors was about 3 mm, as specified [HC-SR04, 2010].



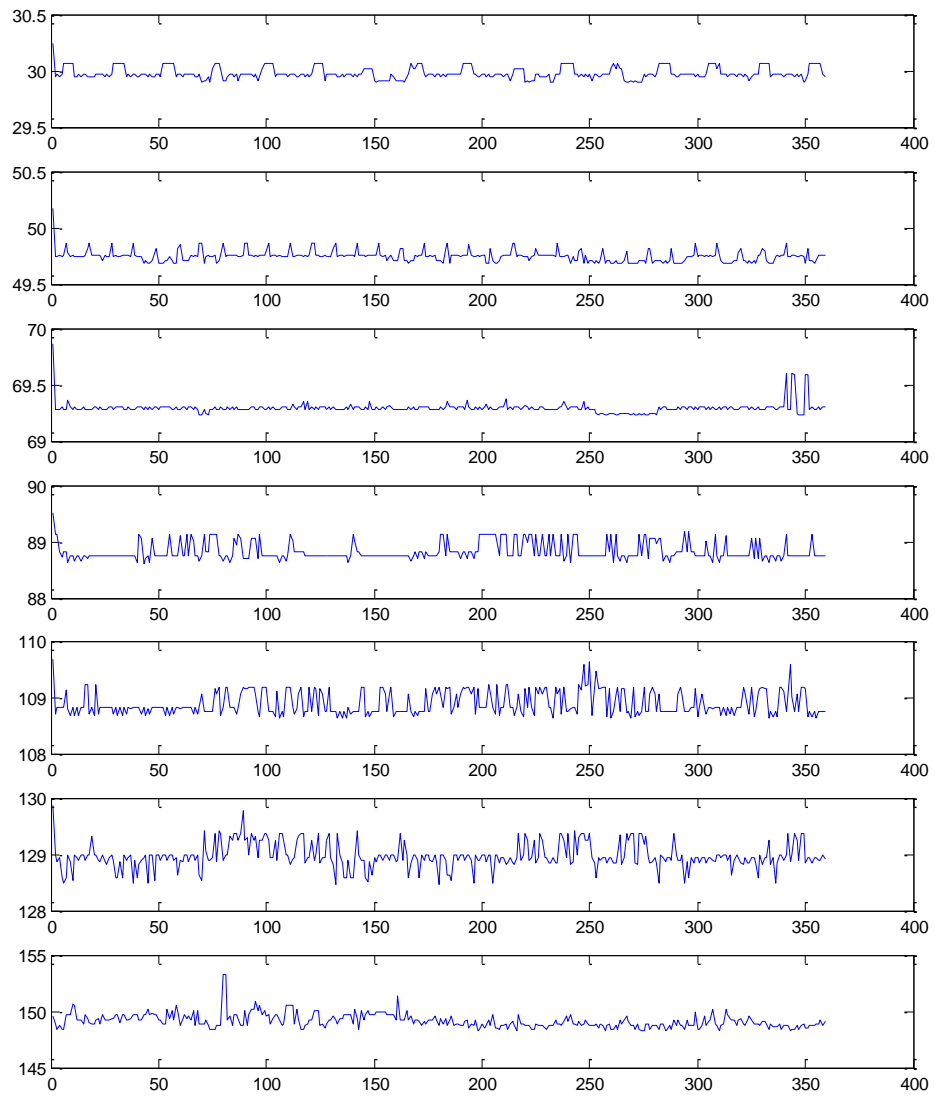


Figure 2-15. Data collection of distances from 20 to 150 cm, with SRS HC-SR04.

Successively, it has been possible to extract the LPTA (landing plane tilt angle) from the four SR04 acquisition; considering Equation (2.5):

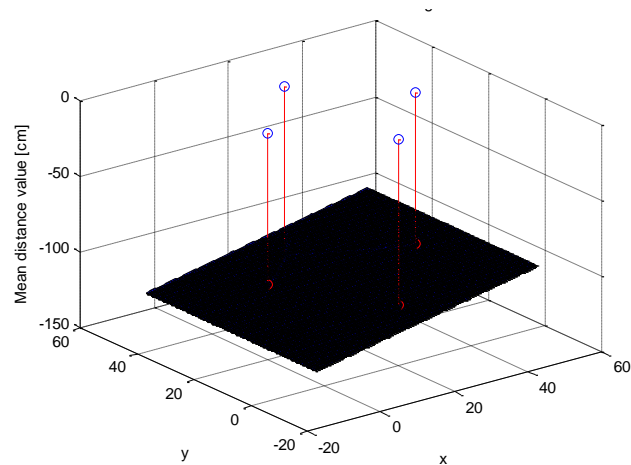


Figure 2-16. Landing Plane extrapolation trough the four SR04 distances.

The system autonomously decides to land or not, evaluating the LPTA and if there were any obstacles around.

In order to cover a wide area, another configuration of ultrasonic sensors was considered. This configuration works like a RADAR, the ultrasonic sensor rotates, thanks to a servomotor, in order to inspect a wide area.

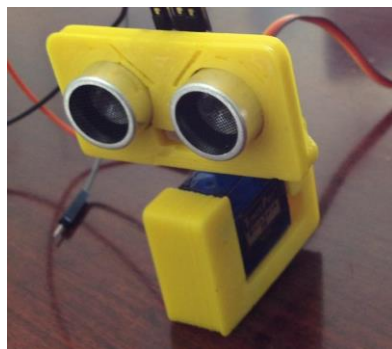


Figure 2-17. HC-SR04 rotary configuration.

In addition, the holding structure was made in ABS (Figure 2-17), designed with a 3D CAD software and printed through 3D printer.

In Figure 2-18 the scanned area contains a box (20x20x20 cm) inside, so in this case the landing was not permitted, because the box height is greater than UAS legs. When an obstacle is detected, as in this case, the user is alerted through an acoustic beep or a blinking led.



Figure 2-18. Obstacle detected in the scanned area.

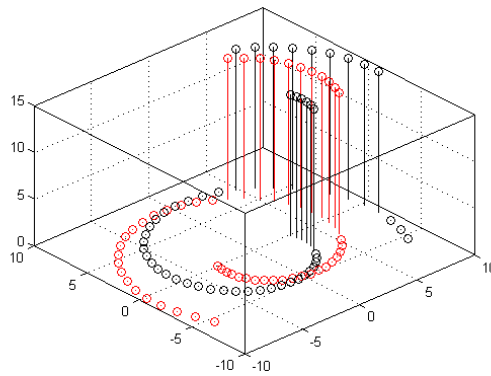


Figure 2-19. Landing field mapping, obstacle detected.

By coupling the ultrasonic sensor with a servomotor, it was possible to generate a map (mapping) in real time like a radar. Considering this hypothesis, a radar display was made, utilizing Processing (a software like Arduino IDE), generating for the user on the GS (ground station) an interactive interface that can detect and show any obstacles in the scanned area, in real time. Figure 2-20 shows ultrasonic radar window.

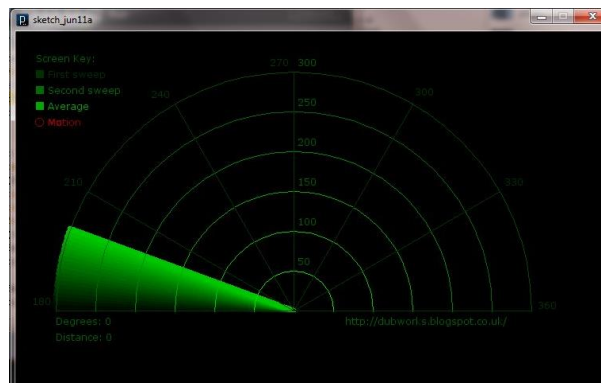


Figure 2-20. Ultrasonic Radar window developed in Processing IDE.

The data collected from the sensors have been processed by the microcontroller, and by means of the Matlab® environment the performance (in Matlab®) and abilities on the arrangements of the HC-SR04 used for UAS application mapping were analyzed. The data from experimental session was directly transmitted, via Bluetooth, to a GS where a computational process was needed in order to implement the mapping procedure. This work was useful in order to estimate and validate the SR sensor (HC-SR04) performance, and build a preliminary system that aids the UAS to land safely.

Next chapter evaluates the atmosphere effects on HC-SR04, generating a mathematical model that enhances the distance measurements extraction, in order to avoid systematic errors.

Publication

The topic discussed in this Chapter has been published.

Papa, U., Del Core, G., (2015). Design of sonar sensor model for safe landing of fan UAV. *Proceedings of IEEE Metrology for Aerospace*. IEEE, pp 346-250.

3. Atmosphere effects on the SRS

3.1 Introduction

Ultrasonic proximity sensors are a good compromise in terms of cost, energy efficiency and accuracy for low distance obstacle detection. Various fields of interest could find this Ph. D. thesis interesting, for example structural damage inspections in critical areas (e.g. L'Aquila earthquake, Italy, or hurricane Ike in Galveston, Texas, US).

Unfortunately, the measurements provided by ultrasonic sensors are affected by systematic errors due to relative humidity and atmospheric conditions. Previous works have dealt with studies concerning specular reflections on ultrasonic sensors (Yi et al., 2000), but they did not consider temperature and relative humidity interactions.

The aim of this chapter is to analyze the effects of temperature and relative humidity conditions on distance measurements provided by ultrasonic sensors, during landing or hovering. The investigations on two commercial ultrasonic sensors (HC-SR04 by Electrofreake and Parallax PING) took place in a small environmental chamber, model KK-105 CH. In order to avoid the systematic errors, two mathematical models have been carried out for both relative humidity and temperature effect compensations.

3.2 Theoretical Framework

The distance measurements provided by SRS are based on the measurements of the time of fly of ultrasonic waves reflected on a target. Considering Equation (2.6) the speed of sound is influenced by atmosphere effects (temperature and relative humidity).

Knowing the numerical value of the sound speed, it is possible to evaluate the distance between the sensor and the target with the following equation (Dean, 1979):

$$d = \frac{c \cdot t_{fly}}{2} \tag{3.1}$$

where t_{fy} is the time interval between the transmission of the ultrasonic wave and the received echo wave and c is the speed of sound.

The Equation (3.1) shows that the distance depends linearly on the speed of sound. If the speed of sound grows more than 10% starting from a nominal value, in the distance measurement occurs an error of 10%. This error can be fatal when finding obstacles during UAS flight.

For a real gas, the speed of sound depends on temperature, pressure, and molecular composition. In classical mechanics, the speed of sound is given by:

$$c = \sqrt{\frac{K}{\rho}} \quad (3.2)$$

where K is the modulus of the bulk elasticity of a gas obtained with the multiplication of the adiabatic index γ and the pressure p , while ρ is the density. If we use the ideal gas law to replace p with nRT/V , and replacing ρ with nM/V , the speed of sound for an ideal gas (c_{ideal}), considering the Equation (3.2), is given by:

$$c_{ideal} = \left[\frac{(\gamma RT)}{M} \right]^{1/2} \quad (3.3)$$

where R is the molar gas constant (approximately 8.3145 J/mol·K), T (K) is the absolute temperature and M_{air} is the molar mass of the gas (for dry air about 0.029 kg/mol).

It is important to specify that, for the mixture air, the molar mass is the average of the mole fractions of its components and their molar masses. If relative humidity changes, there will be a variation of water particles concentration in the air mixture, so that the molar mass changes. This formulation is valid only for small perturbations on the climate condition.

Based on previous equations (Dean, 1979), the speed of sound can be derived according to the following formula:

$$c_{air} = 331.3 + 0.606 \cdot \vartheta \quad (3.4)$$

where ϑ is the temperature in Celsius and 331.3 is the speed of sound (m/s) in dry air (0% humidity) at 0 °C. This formula is derived from the first two terms of the Taylor Expansion:

$$c_{air} = 331.3 \cdot \left(1 + \frac{g}{273.15}\right)^{1/2} \quad (3.5)$$

An equivalent form Equation (3.5) is obtained by multiplying the right hand side by $(273.15)^{1/2}$:

$$c_{air} = 20.05 \cdot (g + 273.15)^{1/2} \quad (3.6)$$

All the above equations show how the distance measurements depend on temperature and gas molar mass (Dean, 1979; Endoh et al., 2003). Hence, it is important to compensate the effect of temperature, relative humidity, pressure and airflow masses during the distance measurements.

3.3 SRSs Testing

The ultrasonic sensors analyzed in this analysis are two low-cost commercial models: (a) HC-SR04, and (b) Parallax PING)))

The first one is described in detail in Chapter 2. The second one, Parallax PING))) (Ping Parallax, 2016) (Figure 3-1a) has a similar range of distance measurement, about 2-300 cm.

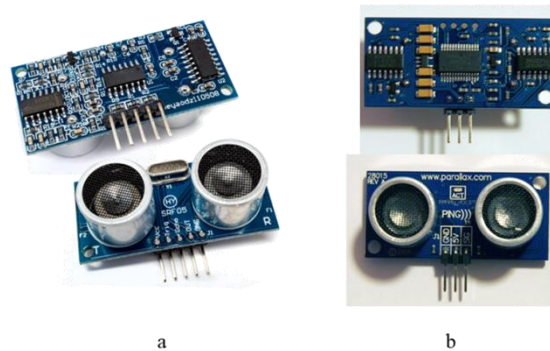


Figure 3-1. a) HC-SR04, b) Parallax PING))).

The shield is quite similar to HC-SR04, but it consists of three pin (Vcc, Ground, IO), where IO includes trigger and echo tasks on one channel. Table 3.1 shows ultrasonic sensors features, in order to evaluate the differences between them.

Table 3.1. SRSs technical chart, according to (Ping Parallax, 2016 & HC-SR04, 2010).

	HC-SR04	Parallax PING)))
Supply Voltage	5V DC	5V DC
Supply Current	15mA	30mA; 35mA max
Range	2-400 cm	2-300 cm
Input Trigger	10 μ s TTL pulse	2 μ s min, 5 μ s typ.
Echo pulse	Pos. TTL pulse	115 μ s to 18.5ms
Burst Frequency	40 kHz	40kHz for 200 μ s
Measuring Angle	< 17° for side	< 20° for side
Dimension	45 x 20 x 15 mm	45.7 x 21.3x 16 mm

The procedure for distance extraction was explained in the Chapter 2.

The position of the sensors have been chosen in order to reduce the interference effects between them. The standing bar and the base were made of wood in order to have a light and stable structure.

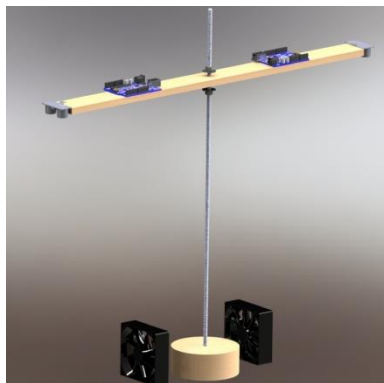


Figure 3-2. Concept of the structure.

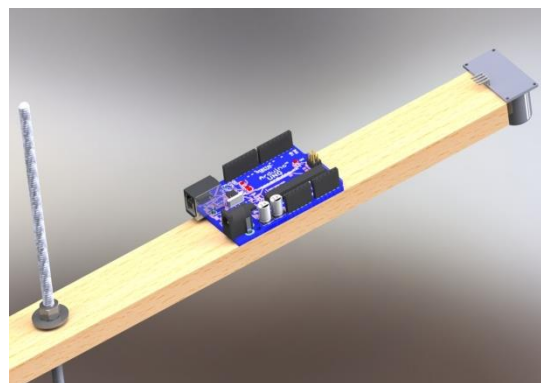


Figure 3-3. Detail: HC-SR04 and Arduino on the wood arm.

3.4 Experimental analysis setup and Results

The aim of this section is to evaluate the temperature and humidity influences on distance measurements provided by ultrasonic sensors.

To investigate these influences, a measurement procedure has been performed in the small size environmental chamber Kambic KK-105 CH (Figure 3-4) with a temperature range from +5 °C to 180 °C, and humidity range from 10% to 98% (Climatic Chamber KK-105, 2016).



Figure 3-4. KK-105 CH Climate Chamber used in this work.

Technical data of the chamber are reported in Table 3.2

Table 3.2. KK-105 CH Technical data (Climatic Chamber KK-105, 2016).

External dimensions (WxHxD) [mm]	725 x 1500 x 845	Uniformity @50°C	±0.5 °C (RH=50%)
Internal dimensions (WxHxD) [mm]	490 x 500 x 430	Control	MPC-PID
Volume [l]	105	Power supply	230 V 50/60 Hz (±10%)
Humidity range	10% ... 98%	Wattage [W]	3000
Humidity stability	±3%	Interface	RS 232
T&Rh display resolution	0.1°C/1%	Weight [kg]	~ 205
Set point resolution T/Rh	0.1°C/1%	Shelve	1 included
Temperature range [°C]	5 ... +180	Access Port	1 x φ 50 mm included
Heating rate	~2.2 °C/min		
Cooling Rate	~ 1.5 °C/min		
Temperature range with humidity control [°C]	+10°C ... +95		

The reference measurement system for temperature and humidity measurements was a certified probe (HD2817T, 2011) model HD2817T (Figure 3-6). In particular, the Leica DISTO™ D3 (Figure 3-5) has been used as reference system for distance measurements.

The tests were made at the LESIM (Laboratorio di Elaborazione Segnali ed Informazioni di Misura – Measurement Information and Signal Processing Laboratory) laboratory at the Department of Engineering of the University of Benevento “Unisannio” (Benevento, Italy).



Figure 3-5. Leica DISTO™ D3.



Figure 3-6. HD2817T , transmitter, indicator, ON/OFF regulator, temperature and humidity datalogger.

Firstly, different cases were considered, in order to analyze the ultrasonic sensor’s performance. Table 3.3 shows the analyzed range, in terms of temperature and relative humidity, for a given set of distances, namely 19, 23, 28, 33 and 38 centimeters, obtaining for each subset a (4x4) matrix.

Table 3.3. Data values setup.

Temperature	Humidity
[°C]	[%]
10	10
20	30
30	50
40	70

All the data were managed through a .vi file (National Instruments, 2003) that let the user configure the procedure parameters. Moreover, the application allows communicating with the microcontroller and the collected data are stored and displayed on the screen thanks to a user-friendly graphic interface (Figure 3-7).

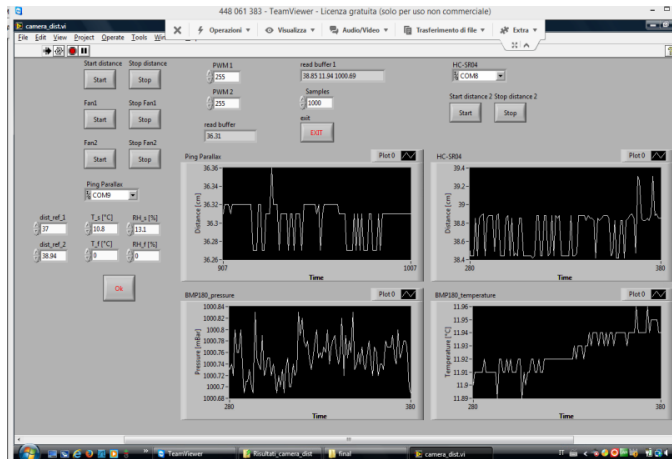


Figure 3-7. Virtual Instrument in LabVIEW™ window (National Instrument, 2003).

Afterward, it is also possible to plot, through Matlab® all collected data during the simulation. In Figure 3-7, it is possible to see how the distance measurements provided by Parallax PING))) depend on temperature and relative humidity for a fixed set distance of 28 cm.

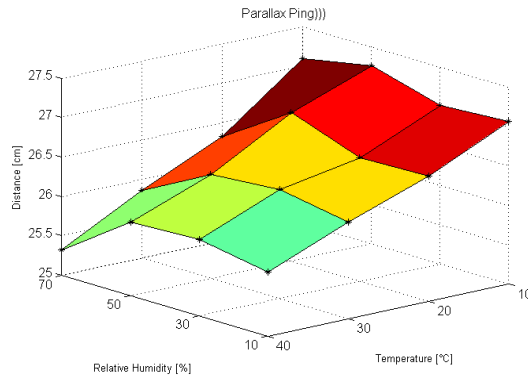


Figure 3-8. Data changing for PING))) Parallax.

In the same way, Figure 3-9 shows the results for the SR04 sensor.

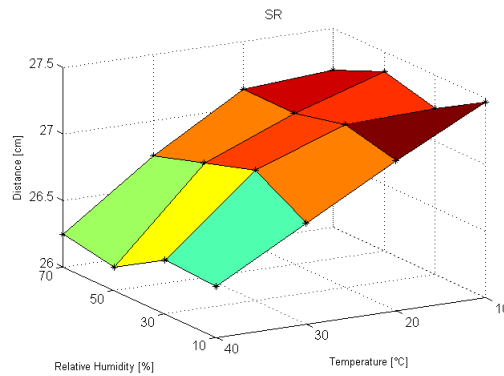


Figure 3-9. Data changing for HC-SR04.

In this case a distance of 28 cm has about 2 centimeters (7%) of variation for a given temperature range (10°C - 40°C), whereas for relative humidity range (10-70%) the distance variation was smaller.

Variations were quite similar for both sensors, otherwise only PING parallax has shown higher measurement stability.

After all these analyses, it was possible to formulate an equation that allows compensating temperature and relative humidity effects on distance measurements. At first, it is possible to perform a linear regression for each measurement provided by the tested sensors compared to the given distance values. The relationship is the following:

$$y = ax + b \tag{3.7}$$

where a and b were respectively the scale factor and the bias coefficient. These parameters depend on the environmental values of temperature and humidity that affect the speed of sound and its formulation (Equation 2.6).

The figures below show the results obtained from the two sensors concerning relative humidity (10%) and temperature (equal to 10 °C). The variation of reference distance was compared to the obtained distance, and the trend of the valued scale factor and bias, were useful to estimate a distance compensation (Equation 3.7).

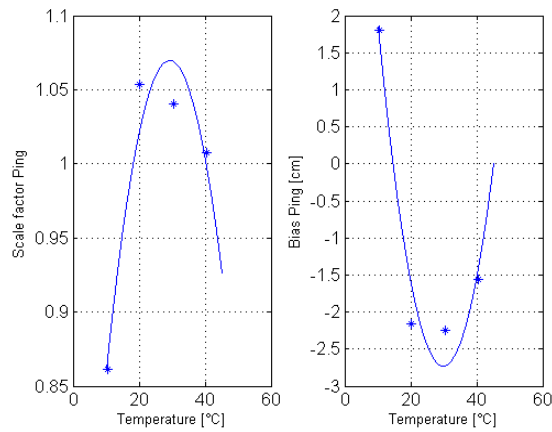


Figure 3-10. Scale factor and bias (RH = 10% - PING).

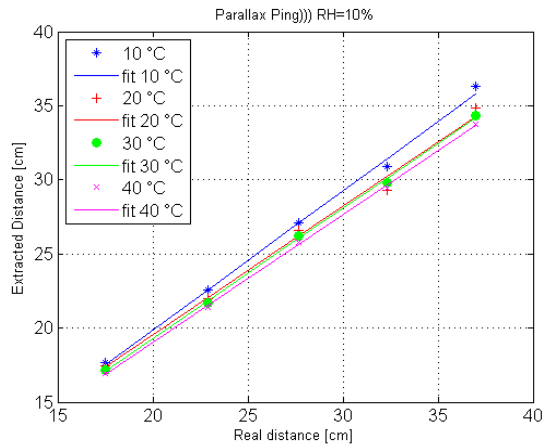


Figure 3-11. Linear function for correction (RH = 10% - PING).

Similarly for the HC-SR04 the procedure:

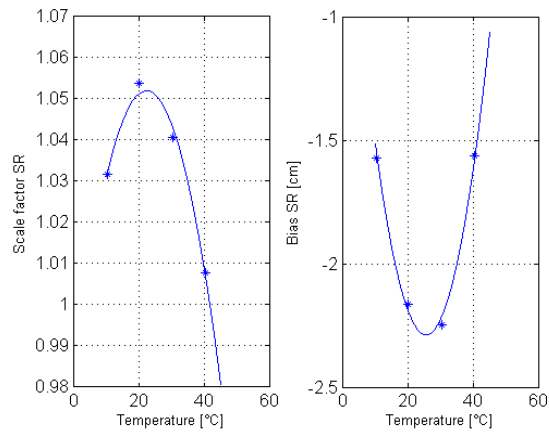


Figure 3-12. Scale factor and bias (RH = 10% - HC-SR04).

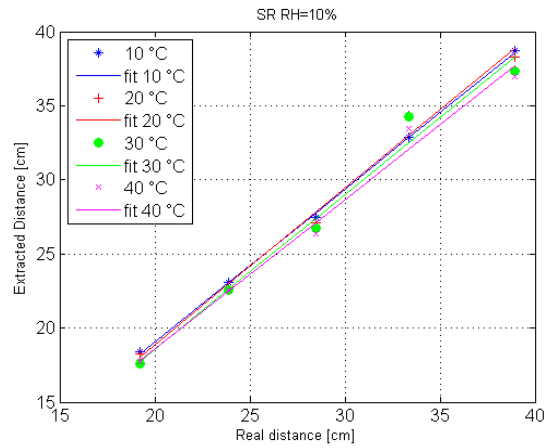


Figure 3-13. Linear function for correction (RH = 10% - HCSR04).

In the previous cases, RH was fixed, whereas in the next cases the temperature was fixed ($T = 10\text{ }^{\circ}\text{C}$).

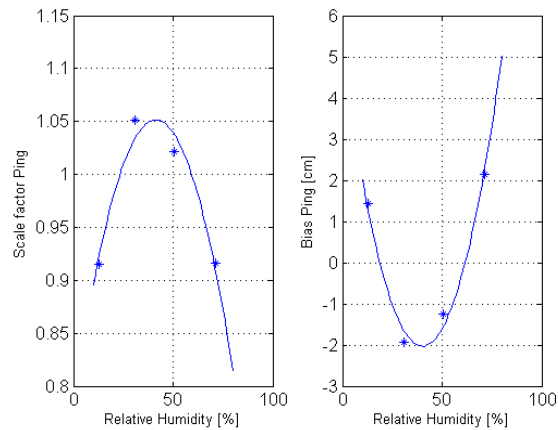


Figure 3-14. Scale factor and bias ($T = 10\text{ }^{\circ}\text{C}$ - PING).

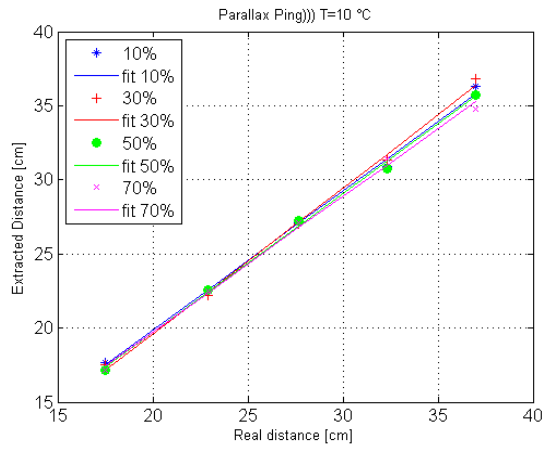


Figure 3-15. Linear function for correction (T = 10 °C - PING).

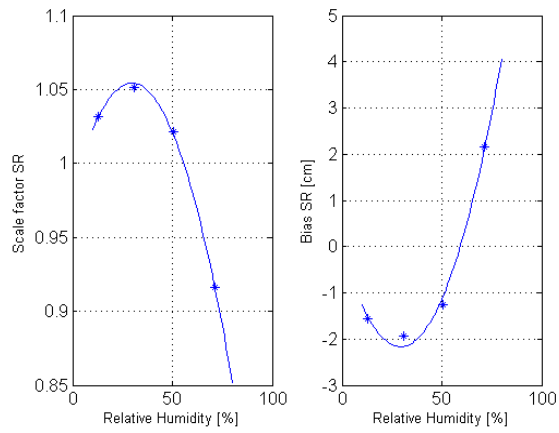


Figure 3-16. Scale factor and bias (T = 10 °C - HC-SR04).

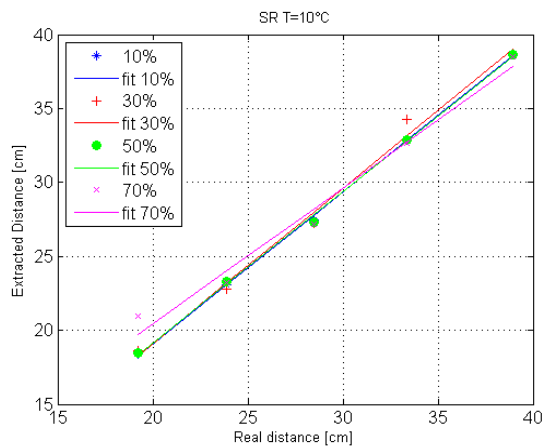


Figure 3-17. Linear equation for correction (T = 10 °C - HC-SR04).

Figures 3.10-12-14-16 show that both scale factors and bias coefficients for both sensors do not change linearly with reference to temperature and relative humidity variations. Therefore, it was important to pay attention to the parameters' choice (scale and bias factor), as closely dependent on temperature and relative humidity calculated during the survey. These parameters are important in order to obtain a good compensation law (Equation 3.7), and an accurate landing or hovering. To appreciate paper contribution, it is useful to evaluate distance errors before and after correction.

Maximum error distance and mean are shown in Table 3.4 below, considering:

- ✦ Distance = 28 cm;
- ✦ Temperature = 20°C;
- ✦ Relative humidity = 30%.

Table 3.4. SRSs comparison before and after the correction.

		maxErr	Mean
		[cm]	[cm]
	Not-Corrected	1.37	26.57
Ping)))	Corrected	0.88	27.88
	Not-Corrected	0.51	27.22
SR04	Corrected	0.21	28.02

The (Equation 3.7) correction was important to obtain a better distance measurement, in real time when temperature and relative humidity may be changing.

3.5 SRSs sensibility

In terms of stability, the PING))) was much stable than SR04, as figures below show for previously discussed conditions.

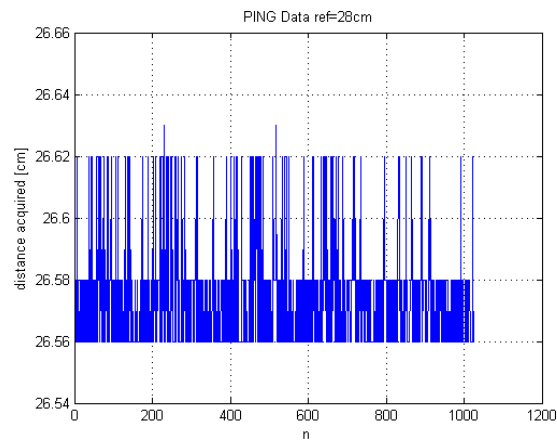


Figure 3-18. PING)) distance acquisition.

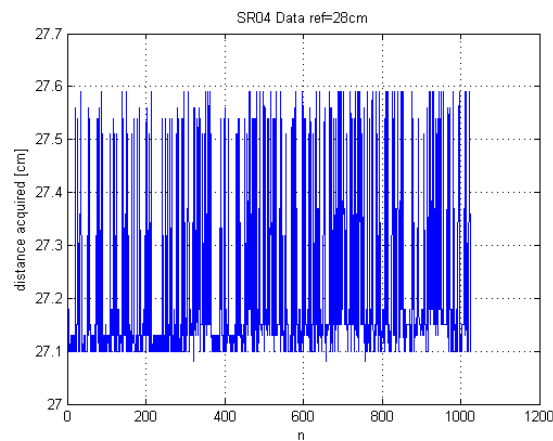


Figure 3-19. HC-SR04 distance acquisition.

Considering an obstacle at 28 cm, the Figures above show that SR04 was better than PING)) in terms of accuracy. The PING)) has a good accuracy but less precision, vice versa the SR04.

3.6 DHT11 Temperature and Humidity Sensor

As has been said, the speed of sound depends on the temperature and relative humidity. In order to estimate their values, a temperature and humidity sensor (Figure 3-20) (DHT11 sensor, 2016) was installed on the platform, managed through the Arduino microcontroller (Figure 2-4).

This sensor includes a resistive-type humidity measurement component and an NTC (Negative Temperature Coefficient) temperature measurement component, and connects to a high-

performance 8-bit microcontroller, offering excellent quality, fast time response, anti-interference ability and a reduced cost.

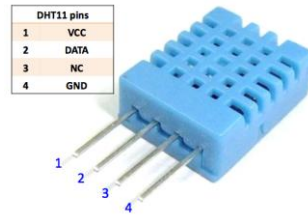


Figure 3-20. Sensor and Humidity sensor DHT11 (pin detail).

The DHT11 communicates through 4-pin (VCC, Data, NC and GND) to the Arduino microcontroller (Figure 3-21).

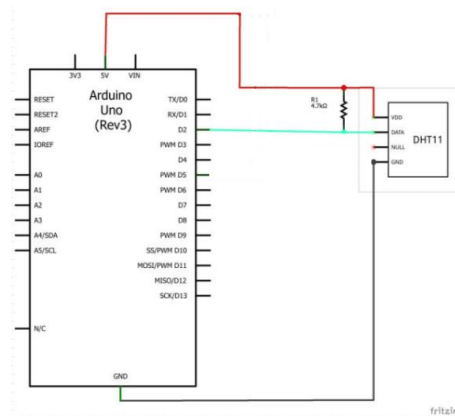


Figure 3-21. DHT11/Arduino Uno (Rev3) electric wiring scheme.

The sensor waits for a low level and then a high level on its data line. Once it detects a low level that lasts at least 18ms and then a transition to a high level again, it initializes its transmission circuitry and pulls the data pin low for 80 μ s as an indication that it will now start sending data. Then it starts the transmission of the readings. It is a total of 40 bits and each bit (1 or 0) is transmitted as a pulse of variable length. If the high level of the pulse is longer than 30 μ s then it is a one. If the pulse is less than 26-28 μ s then it is a zero.

More details on temperature and humidity extraction from signal are reported in the DHT11 library and in (DHT11 sensor, 2010).

Publication

The topic discussed in this Chapter has been published.

Papa, U., Picariello, F., Del Core, G., (2016). Atmosphere effects on sonar sensor model for UAS applications. *IEEE Aerospace and Electronic Systems Magazine*, Vol. 31, Issue 6, pp 34-40.

4. Integration among Ultrasonic and Infrared Sensors

4.1 Introduction

In this Chapter, another distance sensor was considered in order to integrate the distance measurements for a good UAS navigation information (Sobers et al., 2009 & Mustapha et al., 2012). An infrared sensor (IRS) has been considered to extract distance information between UAS and a fixed surface (or obstacle) through infrared (IR) wave bouncing. The IRS distance measurement was useful for a further integration when SRS was out of order or unavailable.

The SRS detects an obstacle like bats or dolphins do, whereas the second one (IRS Sharp) bounces IR off objects to determine how far away they are. The considered distance range is always 30-160 cm, since both sensors work well in this range.

4.2 Infrared Sensor – IRS

The infrared sensor Sharp (GY2Y0A02YK0F) (Sharp, 2006) was chosen in this Ph.D. thesis because it is a miniature, low cost, fast response time sensor, and has good sensing range to detect obstacles.



Figure 4-1. IRS Sharp.

The IRS Sharp is a distance measuring sensor unit, composed of an integrated combination of PSD (Position Sensitive Detector), IRED (infrared emitting diode) and signal processing circuit. The variety of the reflectivity of the object, the environmental temperature and the operating duration are not influenced easily by the distance detection because of adopting the triangulation method. This device outputs the voltage corresponding to the detection distance. So this sensor can also be used as a proximity sensor (Sharp, 2006).

Table 4.1. IRS features (Sharp, 2006).

Distance measuring range	20-150cm
Output type	Voltage
Package size	29.5x13x21.6 mm
Consumption current	Typ. 33 mA
Supply Voltage	4.5-5.5 V

The distance measurement for IRS was provided by a correlation between output voltage and distance. This function is non linear (Figure 4-2). The IRS can calculate the distance from objects up to 150 cm (in this project a range 30-150 cm was used, to realize a landing autonomous procedure).

Preliminary distance extraction, done in experimental data collection, has produced the following graph, confirming the non-linearity.

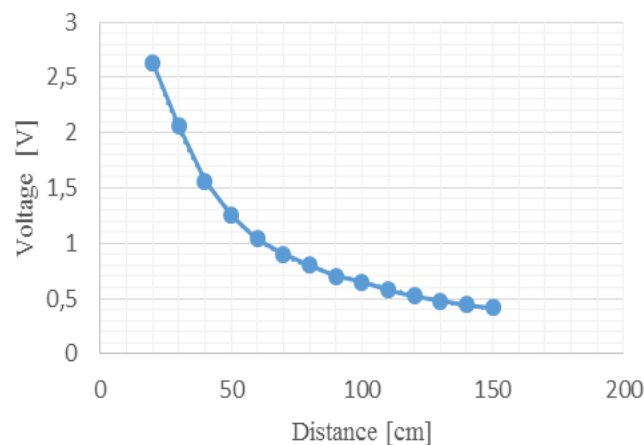


Figure 4-2. IRS voltage acquisition during data collection, considering a range of distances 20-150 cm.

Considering the reciprocal distance-voltage relationship, the function became linear over most of the useful range of the sensor (Figure 4-3). Anyway, log-log scale was an alternative way to linearize and plot nonlinear measurements, but the results were quite similar.

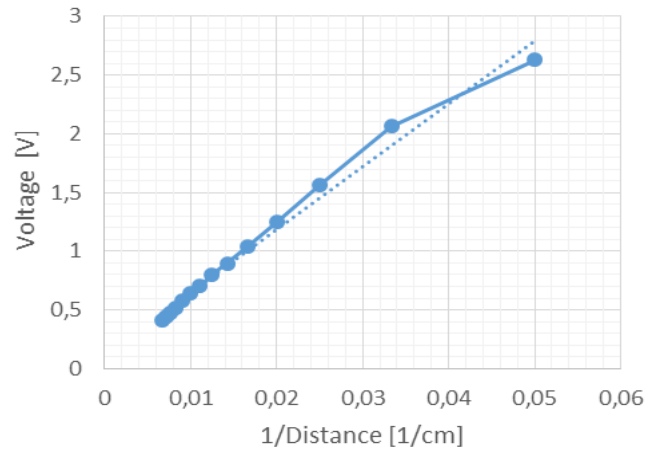


Figure 4-3. Experimental Data collection, (Voltage vs. reciprocal Distance).

The function in Figure 4-3 can be splitted in three linear functions, as shown in the following system:

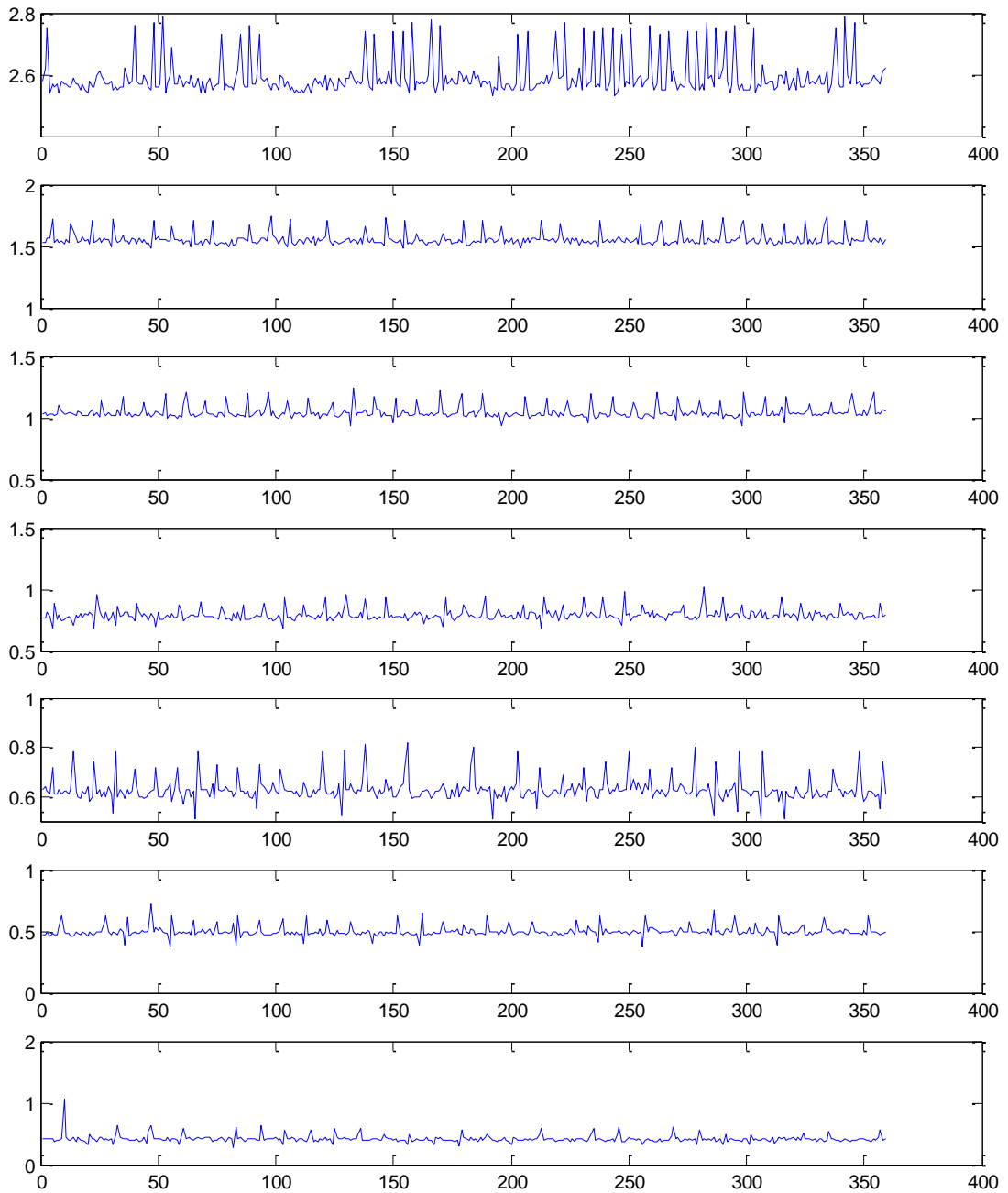
$$\begin{cases} y_1 = 47.689x + 0.3256 & \Rightarrow (20 - 60 \text{ cm}) \\ y_2 = 59.518x + 0.0502 & \Rightarrow (60 - 100 \text{ cm}) \\ y_3 = 69.983x - 0.0573 & \Rightarrow (100 - 150 \text{ cm}) \end{cases} \quad (4.1)$$

where y and x were respectively the voltage and the reciprocal distance. In this way, it was possible to estimate distance from the voltage carefully.

Nevertheless, an alternative function was used, exponential formulation (Equation 4.2), but with less accuracy.

$$y = 61.537x^{-1.048} \quad (4.2)$$

First data collection were made considering a range of distances from 20 to 150 cm, following images shows the voltage data (y -axis) vs. time (x -axis).



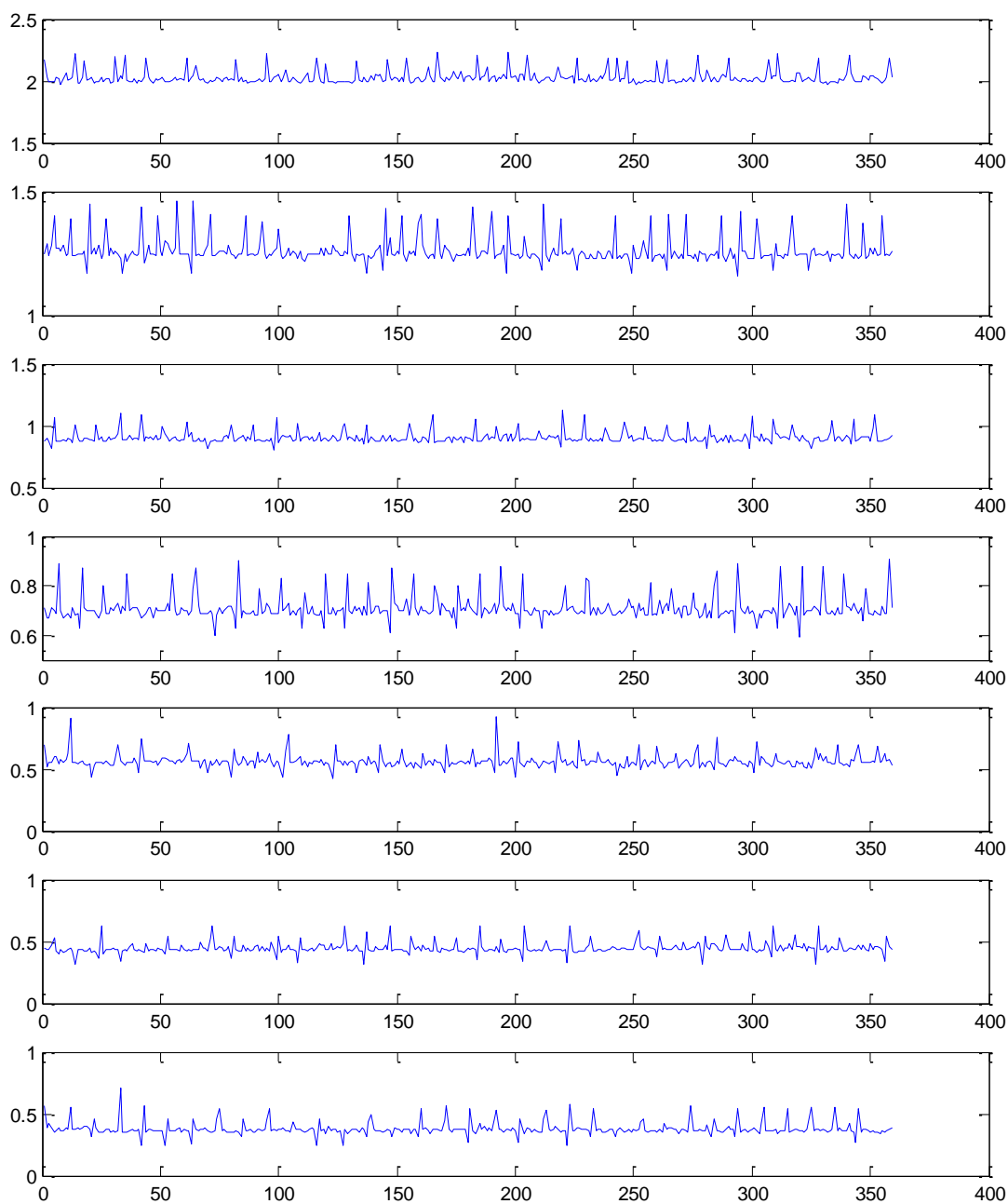
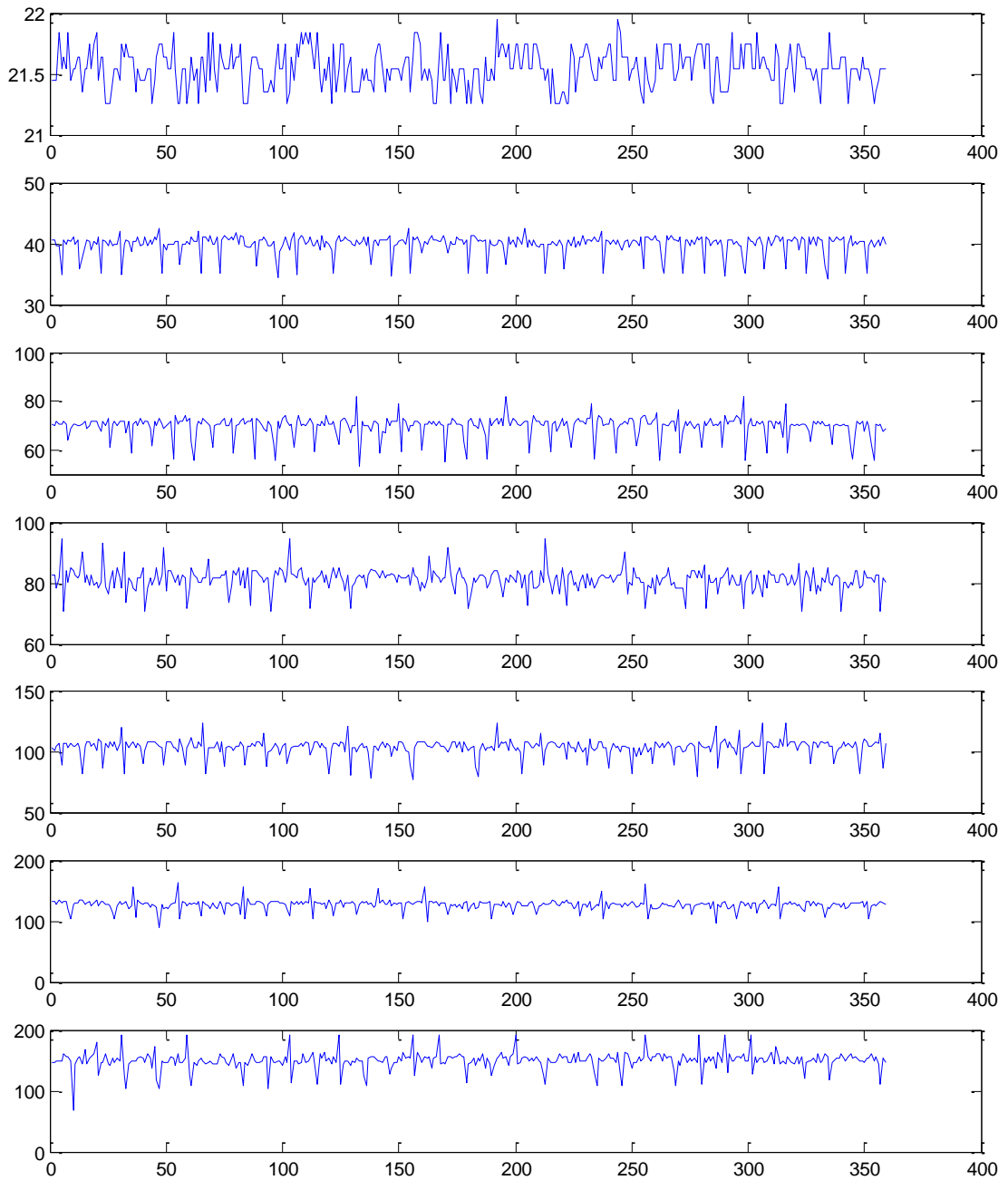


Figure 4-4. Voltage vs. time IRS distance acquisition. Single acquisition time was 6 min (360 sec) @ 1 Hz.

The acquisition time was of 360 seconds for a fixed distance from 20 – 150 cm. The voltage datum was converted in distance data using the Equation (4.1).



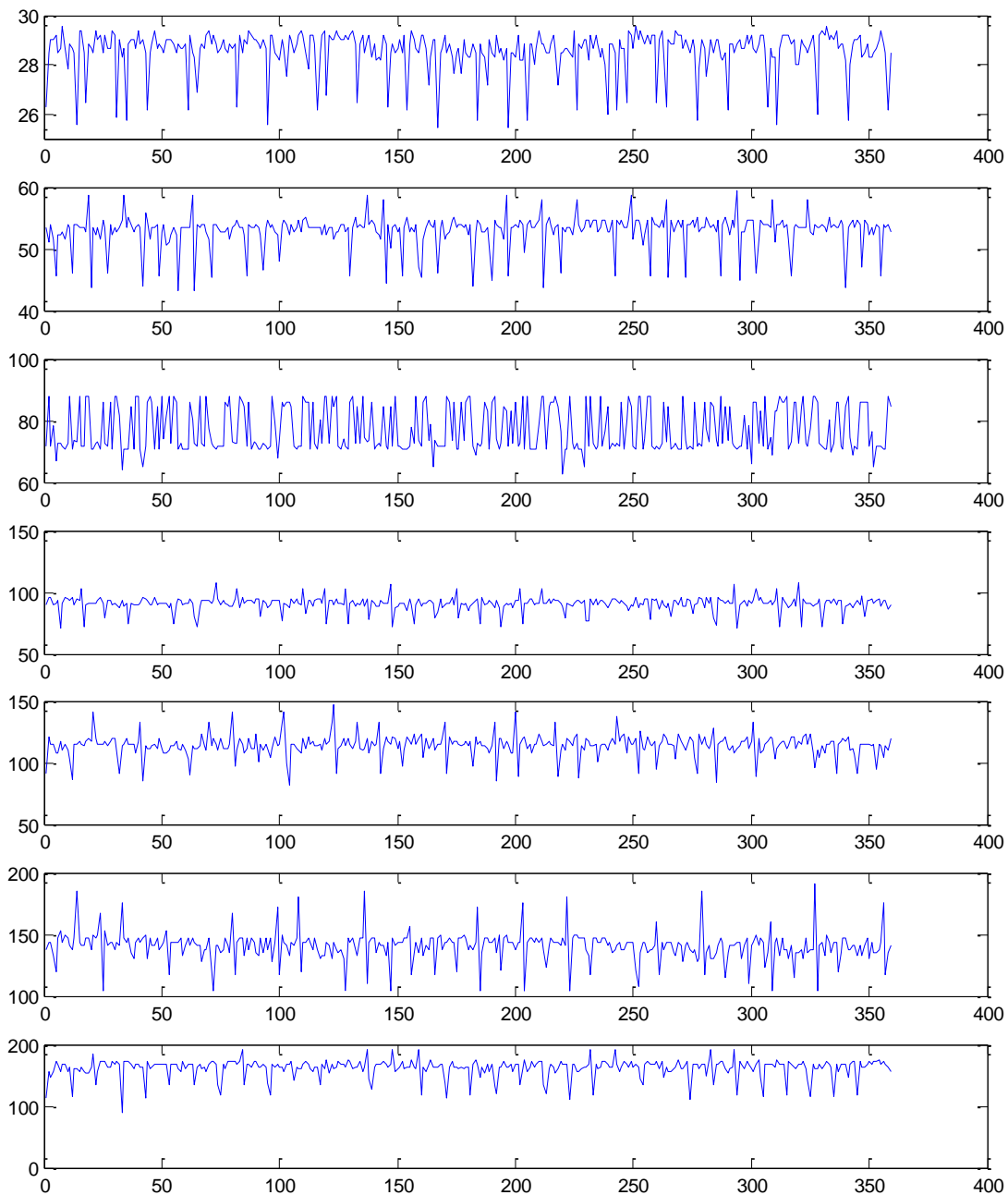


Figure 4-5. Distance vs. time, IRS acquisition. Single acquisition time was 6 min (360 sec) @ 1 Hz.

The IRS was also tested for attitude estimation (Song et al., 2004), in particular during a turn right maneuver (around the roll axes) of the UAS (Figure 4-6). The maneuvers were performed at low velocities and low altitude.

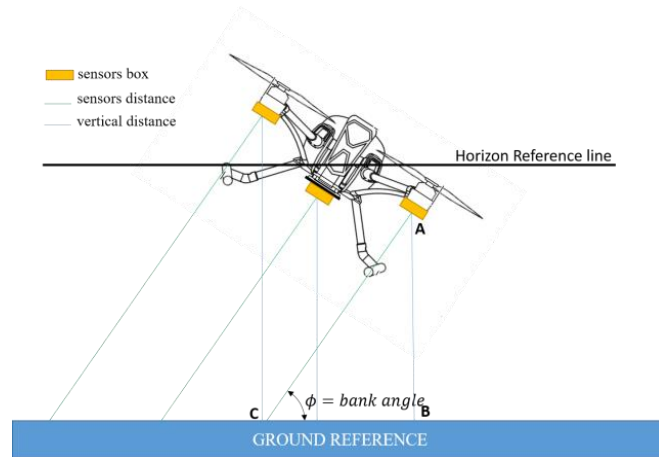


Figure 4-6. IRS and SRS testing during a turn right maneuver.

The distances extracted from IR sensor, during turn right maneuver, were processed considering the ABC triangle (Figure 4-6) and the equations for LPTA (landing plane tilt angle) extrapolation (Chapter 2, §.5).

The resulting plane was depicted in the Figure 4-7:

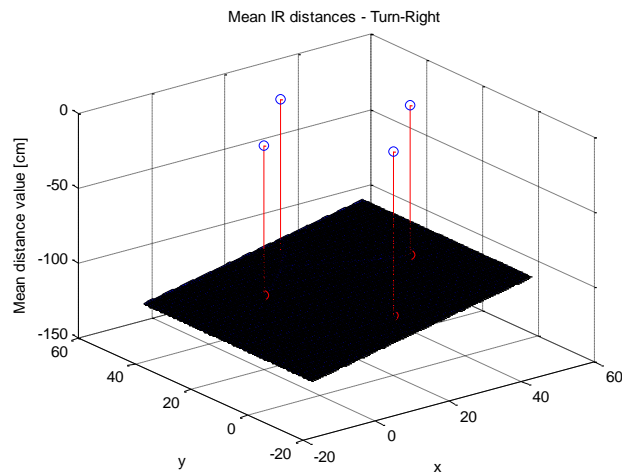


Figure 4-7. IRS distances and extracted plane during Turn-right.

The ground reference (blue plane) was inclined and the sensors (UAS) were horizontally aligned.

Figure 4-8 shows the trend of distance acquired; in this case was considered a distance of 110 cm from the ground.

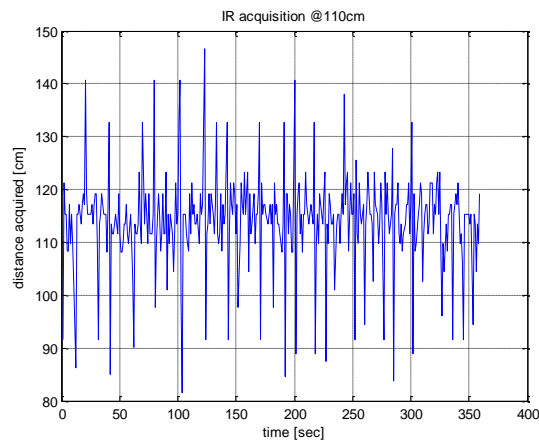


Figure 4-8. IRS acquisitions, UAS at 110 cm from the fixed surface (ground).

The distance extraction procedure, of the SRS has been omitted here, because it was already considered in Chapter 2.

4.3 Sensors data distance integration

In the previous section, sensors for distance acquisition have been described. The IRS and SRS data were read, managed and controlled by an Arduino board, by means of analogical and digital pins. The data were sent from Arduino to PC via serial communication port (or Wireless Shield). The sensors data were read using pulse-width method (PWM) through an interrupt pin on the Arduino board. The electrical scheme in the Figure 4-9 shows overall distance acquisition system (Timmins, 2011).

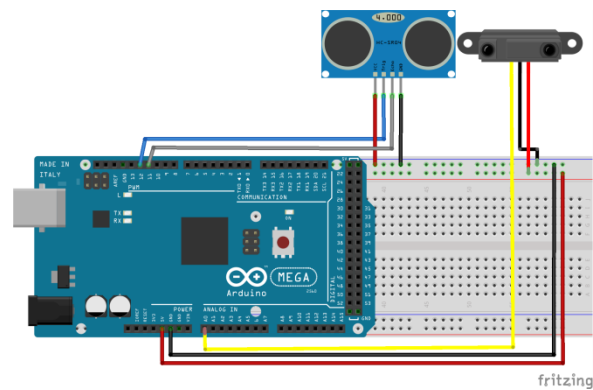


Figure 4-9. IRS and SRS acquisition system and wiring with Fritzing software.

The aim was to acquire and integrate data distances from IR and SR sensors, in this test, a fixed range of 20-150 cm was considered.

The data collection has been divided in step of 10 cm. Each one have a session time acquisition of 3 minutes (180 sec) at a frequency of 2 Hz (one sample each 0.5 second). A total of 360 distances, for each data collection, has been acquired.

The distance datum, for each sensor, was given by:

$$\begin{aligned}x_{SR} &= x + e_1 \\x_{IR} &= x + e_2 \\E(e_1) &= E(e_2) = 0\end{aligned}\tag{4.3}$$

where e_1 and e_2 are the errors committed during the acquisition, considering zero mean and standard deviation σ_1 and σ_2 .

The IRS and SRS distance measurements have been used to obtain an optimal value \hat{x} , which minimizes the relative variance (Gelb, 1974).

A weight p , was associated with each measurement considering the mean value between them as follows:

$$\bar{x} = \frac{p_1 x_1 + p_2 x_2}{p_1 + p_2}\tag{4.4}$$

placing:

$$w = \frac{p_2}{p_1 + p_2}\tag{4.5}$$

so:

$$\bar{x} = x_1 + w(x_2 - x_1)\tag{4.6}$$

Where w is the weight that suppose a variance minimization. If we consider mean and variance of \bar{x} , as $E(\bar{x})$ and $E[\bar{x} - E(\bar{x})]^2$:

$$E(\bar{x}) = E(x_1) + wE(x_2 - x_1)\tag{4.7}$$

If replace the Equation (4.7) in the variance formulation for \bar{x} :

$$\begin{aligned} \sigma^2 &= \{(1-w)[x_1 - E(x_1)] + w[x_2 - E(x_2)]\}^2 \\ \sigma^2 &= (1-w^2)\sigma_1^2 + w^2\sigma_2^2 \end{aligned} \tag{4.8}$$

Minimizing the variance σ^2 :

$$\frac{\partial \sigma^2}{\partial w} = -2(1-\hat{w})\sigma_1^2 + 2\hat{w}\sigma_2^2 = 0 \tag{4.9}$$

where:

$$\hat{w} = \frac{\sigma_1^2}{\sigma_1^2 + \sigma_2^2} \tag{4.10}$$

Considering the Equation (4.6):

$$\hat{x} = x_1 + w(x_2 - x_1) \tag{4.11}$$

In this experimental sessions, x_1 and x_2 are respectively x_{IR} and x_{SR} , thus, it was possible to integrate IRS and SRS measurements.

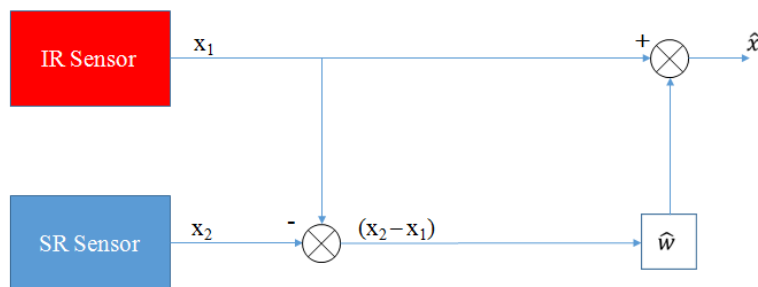


Figure 4-10. Block diagram for integration.

4.4 Simulation and Results

The proposed system has been tested successfully for indoor/outdoor environment. The experimental campaign has been performed in the Flight Dynamics Lab of the University of Naples “Parthenope”; the distance measurement platform was installed on a test bench, then measurements were made with the sensors installed on board of the UAS. Two different cases were considered:

- ✦ Measurements in International Standard Atmosphere (T=15°C, pressure=1013mbar, dry air);
- ✦ Measurement at ISA+20°C (considered as a worst condition).

In accordance with previous section, considering Equation (4.10) and Equation (4.11):

$$\hat{x} = x_{IR} + w(x_{SR} - x_{IR})$$

$$\hat{w} = \frac{\sigma_{IR}^2}{\sigma_{IR}^2 + \sigma_{SR}^2}$$

The measurements were done by moving a white paper box along a path, which covers the range of distances initially considered (20-150cm).

Different colors of the box were considered, but the results were quite similar (Mustapha et al., 2012). The voltage-distance characteristic obtained in each data session from 20 to 150 cm, from infrared sensor is shown in Figure 4-2, according with Equation (2.2). The characteristic was converted in distance acquired-distance graph, where distance is the “*true distance*” measured through a Leica DISTO™ 3 (laser distance meter - Figure 3-5).

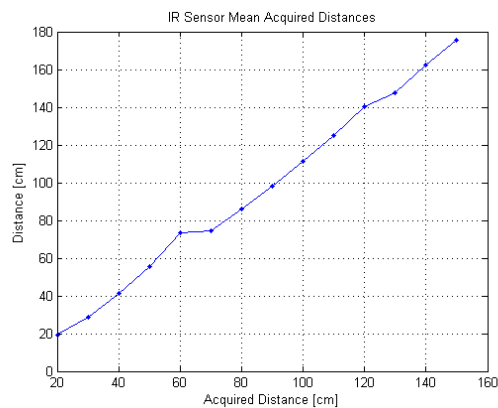


Figure 4-11. Measurements results for IRS.

The standard deviation σ and the variance σ^2 of IR sensor were then calculated (Figure 4-12).

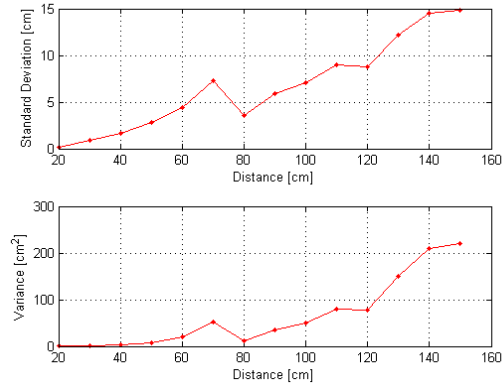


Figure 4-12. Standard deviation and variance for IRS.

For the IRS, the variance and the standard deviation increase, according to the distance of the detected object.

The same procedure was done for SRS (HC-SR04).

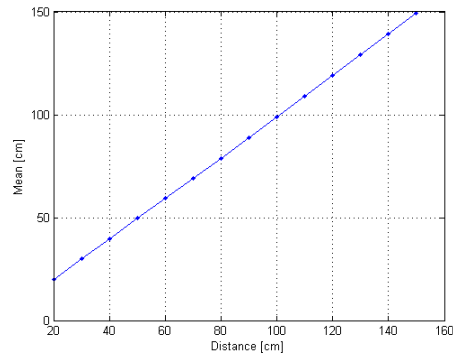


Figure 4-13. Measurement results for SRS (HC-SR04).

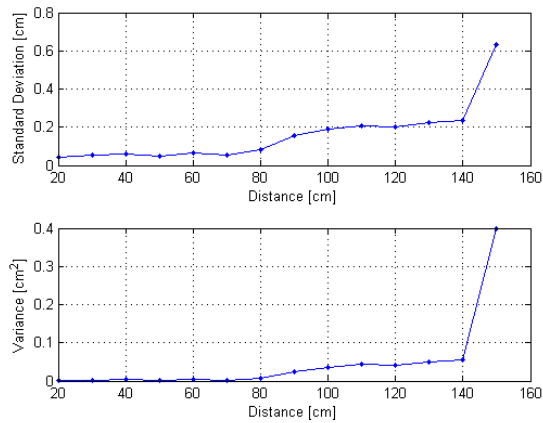


Figure 4-14. Standard Deviation and variance of SRS.

As mentioned, if the object is closer, the error of both sensors, even in this case, decreases. In ISA conditions, the SRS sensor seems to be better than the IRS. It will be useful to integrate both distances measurements, thanks to the Equation (4.10) and Equation (4.11).

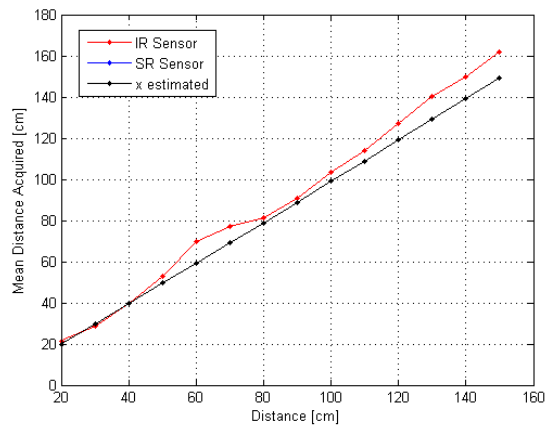


Figure 4-15. Mean of SRS, IRS and x estimated comparison (@ISA).

The ISA conditions are reported in Table 2.2.

In Figure 4-15 *x-estimated* refers to the estimated distance obtained due to Equation (4.11).

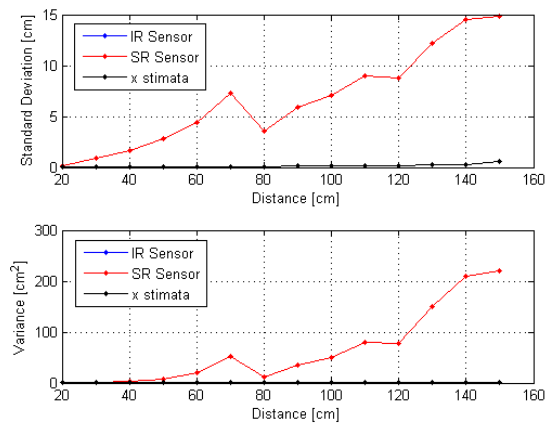


Figure 4-16. Standard Deviation and Variance comparison (@ISA).

The Figure 4-14 and Figure 4-15, show how \hat{x} (IRS+SRS integration), improves distance data. In this case, the IRS measurements were insignificant. Table 4.2 shows RMS (Root Means Square) and max distance error between IR, SR and the integrated data distance \hat{x} .

Table 4.2. Error comparison in ISA conditions.

	IRS	SRS	\hat{x}
RMS [cm]	6.4325	0.8489	0.8248
maxErr [cm]	11.705	0.192	0.116

The distance improvement, given by \hat{x} , in this case is minimal.

A worst-case scenario was considered, increasing the temperature, from 15° to 35°C.

In this case, both sensors do not work correctly. However, with IRS+SRS integration this problem will be bypassed.

The data collection results show that the distance integration \hat{x} , in this case, improves. In the meantime, the temperature influence on SRS is visible in the following figures:

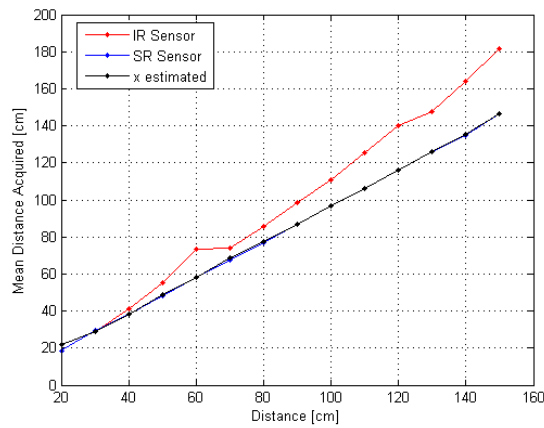


Figure 4-17. Mean of SRS, IRS and x estimated comparison (@ISA+15).

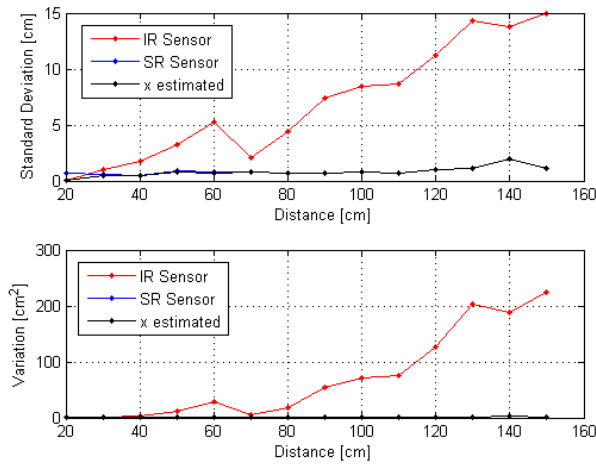


Figure 4-18. Standard Deviation and Variance comparison (@ISA+15).

Table 4.3, as Table 4.2, shows RMS (Root Means Square) and max distance error between IRS, SRS and integrated data distance.

Table 4.3. Error comparison @ISA + 15.

	IRS	SRS	\hat{x}
RMS [cm]	14.643	3.093	1.587
maxErr [cm]	21.437	0.6089	0.1910

In this "worst-case" the RMS and the max Error on the SRS/IRS nearly redouble. The enhancement was only 1.5 cm, but this distance was enough in order to improve a position correction during the small UAS landing.

This integration was useful for a first enhancement of the distance measurements when SRS is out of order or unavailable.

Further work will consider the sensor fusion using a Kalman filtering, and the use of additive sensors like optical sensors, discussed in next chapter.

5. UAS safe landing using an optical sensor and the space resection method

5.1 Introduction

The installation of an optic sensor (i.e. camera) to an UAS allows the vehicle to perform a variety of tasks autonomously (Valanakis, 2007). This Chapter presents UAS vision system developed and tested at the University of Naples Parthenope to perform an aid for the UAS during the landing procedure at low altitude.

Visual sensors, such as electro-optic or infrared cameras, have historically been included in the on-board equipment of many UASs to increase their value as a surveillance tool.

An autonomous vision-based landing system for small quad-rotor was designed and developed (Sharp et al., 2011). The system uses a single camera to determine the precise position and orientation respect a well-defined landing pattern. Indeed, the developed procedure is based on photogrammetric Space Resection Solution (SRS), which allows determining a single camera position and orientation starting from at least three reference control points, not aligned, whose image coordinates may be measured in the image camera frame. Obviously, the computation of 3D position and attitude parameters of UAS are carried out in the reference system of control points, and they can easily expressed in a global reference system. A specific landing pattern with five circular coloured targets was realized, therefore for each image, the 2D image frame coordinates of the target centre were extracted through a particular algorithm. The centre and radius of the circular coloured target was found by using Hough Transform Function algorithms.

The aim of this section is to compute UAS precise position, from single image, in order to have a good approach to landing field. This procedure is helpful when the GPS module is out of order or a sufficient number of satellites are not available, otherwise GPS tracking can be used for landing position correction. Furthermore, this procedure can be applied when the landing field is movable; the UAS will follow the landing pattern until the landing phase is closed.

5.2 Vision-based embedded system

In this section is explained how to search location and orientation of on-board camera, especially for a quad-copter UAS, through a vision-based methodology. In particular, the Space Resection Method (SRM) used in photogrammetry is adopted. The approach performs a set of landing path coordinate corrections, in order to have an accurate path of descent in a specific area, aided by a landing pattern on the ground positioned. Thus, the UAS receives from the system a track correction (x, y, z) for overall landing procedure. The corrections are sent to the autopilot system, but this is not dealt in this work. Finally, it is important to specify that the overall system is embedded on board, and on the ground there is only a landing path that contain a specific coded target.

The whole system is composed by:

- ✦ Camera module – Raspberry Pi camera module;
- ✦ Mini computer - Raspberry Pi mod. B.

5.2.1 *Camera*

The camera module used in this project is RPI CAMERA BOARD i.e. Raspberry Pi camera module as shown in Figure 5-1 (Raspberry Pi Camera, 2016). The camera plugs directly into the CSI connector on the Raspberry Pi. It is able to deliver clear 5MP resolution (2592x1944 pixels) images due to a Omnivision 5647 sensor in a fixed-focus camera that supports HD 1080 p30, 720 p60 and VGA90 video modes, recording respectively at 30, 60 and 90 frames per second. The module attaches to Raspberry Pi, by means of a 15-pin ribbon cable, to the dedicated 15 pin MIPI Camera Serial Interface (CSI), which is specifically designed for interfacing to cameras. The CSI bus is capable of extremely high data rates, and it exclusively carries pixel data to the BCM2835 processor. This camera works with all models of Raspberry Pi 1 and 2 (Figure 5-2). It can be accessed through the MMAL and V4L APIs, and there are numerous third party libraries built for it, including the Picamera Python library. The picamera package (Picamera, 2013) provides pure Python interface to the Raspberry Pi camera module for Python 2.7 (or

above) or Python 3.2 (or above). Programmable controls for frame rate 32 bytes of embedded one-time programmable (OTP) memory and Digital video port (DVP) parallel output interface.



Figure 5-1. Raspberry Pi Camera Board, it works with all models of Raspberry Pi 1 and 2.



Figure 5-2. Raspberry Pi 2 mod. B.

5.2.2 Landing System Design

On the UAS, an embedded platform is designed. It contains the whole hardware, in order to make image acquisition for data extrapolation. The Raspberry camera module, Raspberry pi and sensors were attached under the UAS. The camera module is connected to the CSI port (Figure 5-3), located behind the Ethernet port, and enable the camera software.

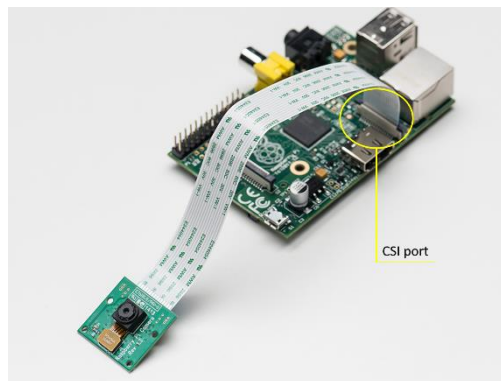


Figure 5-3. CSI port connection between Raspberry and the Camera module.

Figure 5-4 shows a scheme of the on-board landing system and the applied sensors.

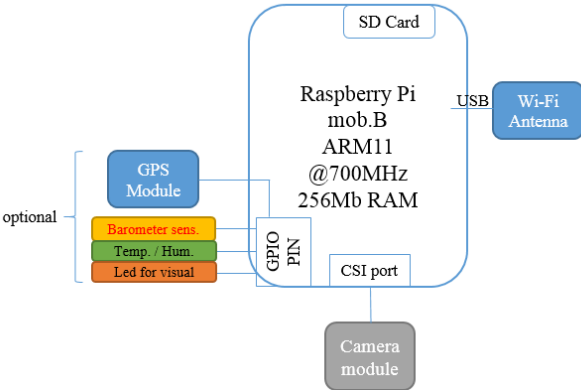


Figure 5-4. On-board vision system scheme.



Figure 5-5. On board vision system.



Figure 5-6. Detail of camera module mounted onboard.

The system works in a standalone mode, a microcontroller ARM11 running @700MHz processes the algorithm. The sensor suite (optional) of landing platform consists of a low-cost pressure, temperature and humidity sensors. For evaluating the current vertical coordinate we use barometric height measurement @MSL, alternatively it is possible to use an Ultrasonic Sonar Sensor designed in previous works (Papa et al., 2015). Furthermore, it is possible to add a GPS module to extract correct altitude and position of the UAS for data comparison and merging.

On this system, OpenCV libraries that allow extracting target contour and coordinates in the acquired current image are available. A basic test landing field, depicted in Figure 5-7, was used.

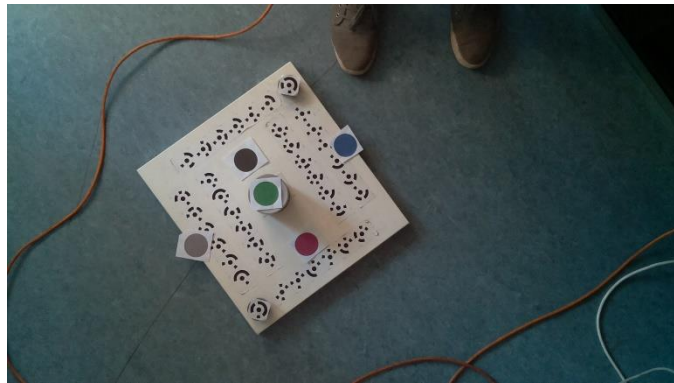


Figure 5-7. Basic Landing Pattern.

The software is able to recognize circular target, filtered by color, and extract its coordinates (in pixel). This was possible through Circular Hough Transform Function. These functions were developed due to OpenCV libraries. The input parameter for good image circle finding is radius range into images acquired; it depends on range of altitudes of UAS (in this case 20-150cm).

Figure 5-8 shows coordinate extracted in real time.

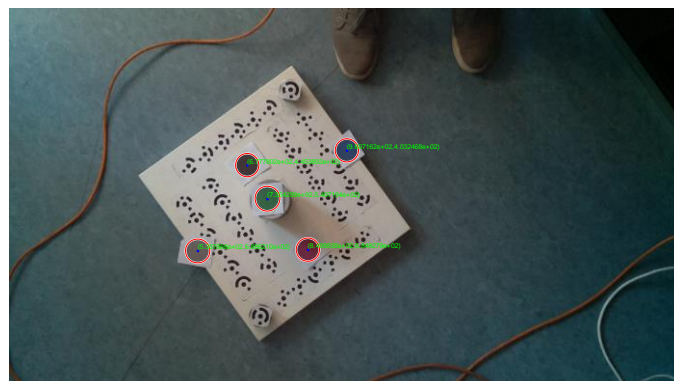


Figure 5-8. Target reconnaissance on pattern.

The range of altitude was the same used throughout the thesis, i.e. from 20 to 150 cm. It is important to remember that this range was typical for a characterization of the UAS during the landing procedure.

5.3 Camera position and attitude extraction

The vision-based landing system is based on the processing of a single image. The goal was to detect camera orientation parameters (position and attitude) in a fixed reference system.

The realization of the reference system was obtained from a special landing pattern. Indeed, the determination of full orientation assumes the availability of enough information in the object space. The mapping of a point x in the object space into a point x' in the camera space (expressed in homogenous coordinates) is fully described by a projection matrix P (Luhman, 2011):

$$x' = Px \quad (5.1)$$

The projection matrix is a 3x4 matrix, which describes the orientation of a pinhole camera. In photogrammetry, the orientation is divided in two different type:

- ✦ External orientation, that describes the position and the attitude of a camera;
- ✦ Internal orientation, that describes the internal camera parameters such as focal length, sensor size etc.

Both these parameters are absorbed in the projection matrix.

In photogrammetry, two methods are known to compute the correct orientation of a single camera starting from object coordinate points and the homologous in camera space: Direct Linear Transform (DLT) and Space Resection Method (SRM).

The former computes directly the projection matrix, solving a linear system, but it needs at least six corresponding image and object points. Furthermore, the solution is not possible if the object points are coplanar (Faugeras, 1993).

The Space Resection Method is not linear, but it assures a solution with only three points not aligned. Furthermore, the theoretical precision of SRM is better than the DLT.

We designed and implemented a vision system for a quad-copter UAS which estimates its relative position and attitude from landing field. Our vision system uses customized vision algorithms. Based on the SRM. All procedures for a correct landing occur in the following stages (Luhman, 2011):

- ✈ Camera calibration to compute all internal orientation parameters;
- ✈ Image coordinates point extraction (image space);
- ✈ Computation of external orientation parameter extrapolation (orientation phase using SRS);
- ✈ Interior orientation parameters were extracted from calibration procedure of the camera;
- ✈ Exterior orientation parameter were extracted thanks to space resection method (SRM) through a non-linear solution.

The following sections describe the overall system setup and the initial procedure needed for correct data extraction.

5.4 Camera Calibration

In order to obtain external orientation parameters with good accuracy, it is mandatory to calibrate the camera. Calibration is the process that allows determining the interior orientation of a camera and the distortion coefficients.

In particular:

- ✈ Principal point or image center (x_0', y_0');
- ✈ focal length (f);
- ✈ radial distortion coefficient (K_1, K_2).

One of the most used analytical camera calibration techniques was originally developed by Brown (Raspberry Pi Org, 2016). This method is often used in close-range photogrammetry to obtain the internal parameters with high accuracy.

The Raspberry camera module (Figure 5-1) is able to fix the focal length and acquire a photo every second in full resolution mode (about 5 Megapixel). To avoid buffer overload and computation errors, and to obtain images with low brightness, the resolution was set to 1920x1080 (about 2 Megapixel), according to an HD video.

The calibration was carried out using a set of coded circular ring-coded target (Figure 5-9), about 40, in order to obtain subpixel precision and to automatize the procedure of calibration.

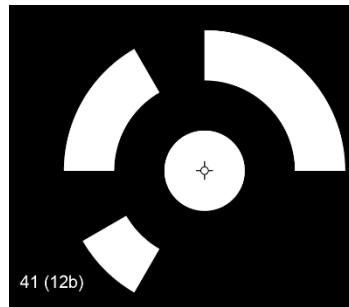
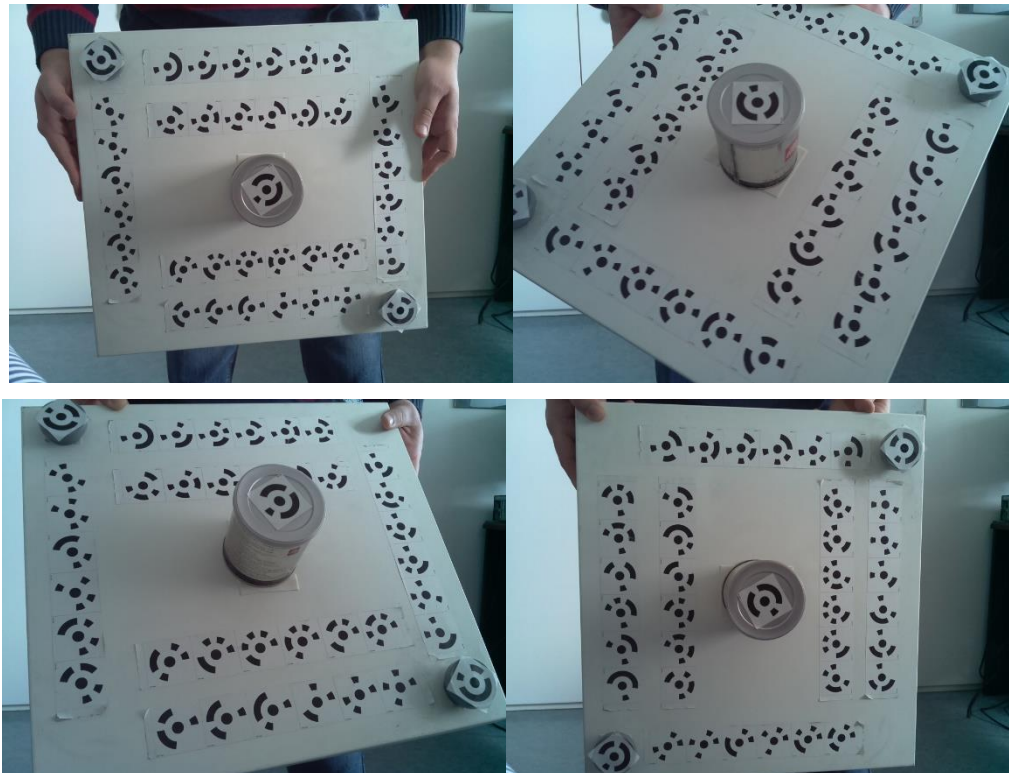


Figure 5-9. Circular ring-coded target useful for camera calibration.

Several frames were acquired for the calibration procedure; in detail, eight images were acquired. They should depict the test field perpendicularly and obliquely and each image should have a relative rotation of 90° around the optical axis.

The following figures show the frames utilized for the calibration procedure.



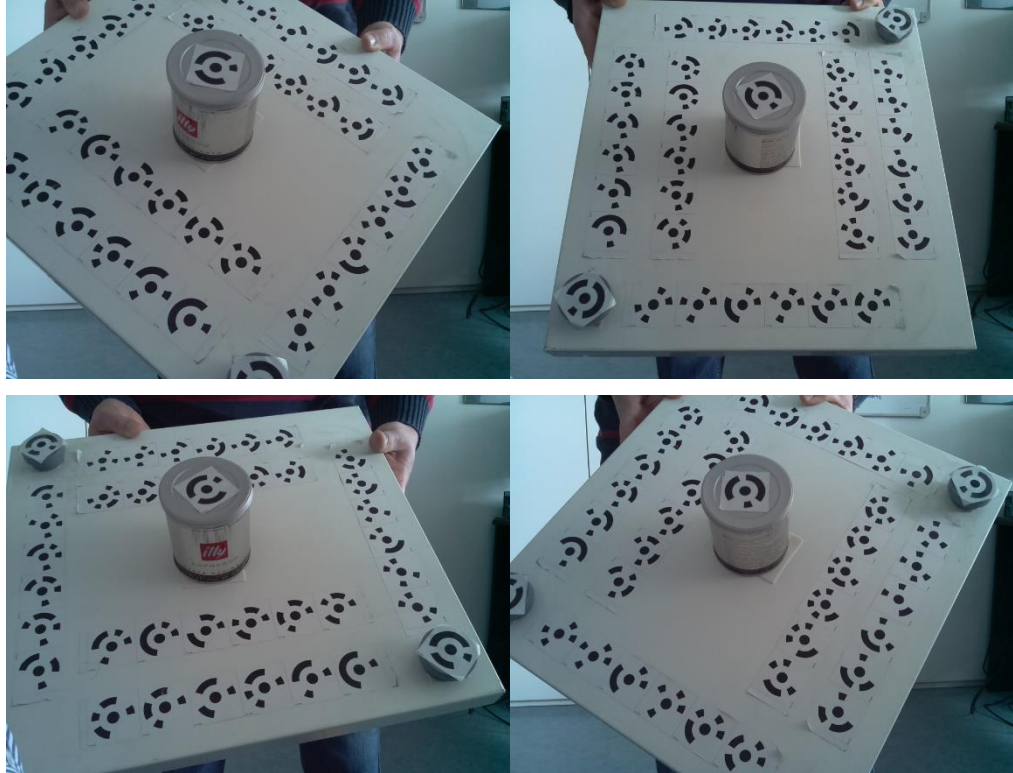


Figure 5-10. Calibration frames.

The Table 5.1 shows the results of the calibration procedure.

Table 5.1. Internal orientation parameters of raspberry camera module.

Camera Name	Raspeberry Camera Module	Standard Deviation
Focal Length [mm]	5.9409	0.003
Sensor Size [mm]	Wide: 6.0035 High: 3.3750	0.006 0.005
Principal Point [mm]	X: 2.997 Y: 1.6808	5.5e-14
Lens Distortion	K ₁ : -1.973e-003	1e-004
Radial Coefficients	K ₂ : 1.653e-004	1.9e-005

The 3D camera network extracted from the camera calibration is depicted in the following figure:

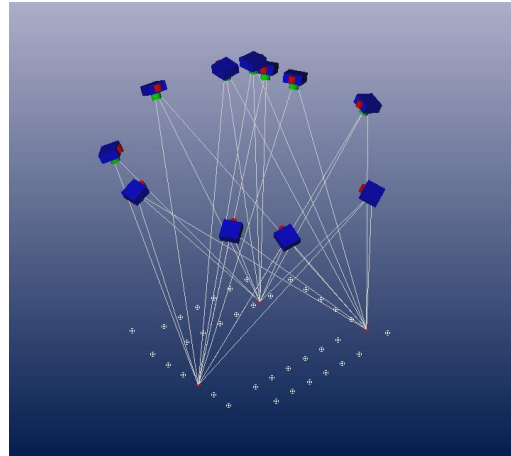


Figure 5-11. The 3D camera positions during the calibration procedure.

The crosses, located at the centre of circular targets, allow one to obtain easily precise measurements of the distances between the targets.

The detected circular coded-target are also visible in Figure 5-12.



Figure 5-12. Detected target in a frame.

5.5 Points Extraction

Object recognition is an important task in computer vision -it identifies a specific object on image. Both SRM and DLT methodologies need to identify the ground control point (GCP) position on the image frame.

In order to solve this problem a specific landing pattern, employing circular target, was developed. Circular targets were designed both to facilitate automatic detection and to assure

good marking accuracy; indeed, it is well known that sub-pixel accuracy can be achieved. All the measurements were referred to the centre of circular target.

Several methods exist to automatically detect the circular targets on image and to find the centre. They can be divided in two categories:

- ✈ No-initial-approximation-required methods. These approaches allow to obtain coordinates center of a circular target on image without any initial approximation;
- ✈ Initial-approximation-required methods. These approaches start from an approximated position of the target center and are able to detect the center with high accuracy.

Of course, the target coordinate center was not sufficient to detect the correspondent GCP. The matching was performed using a unique code for every target. In this work, the codification was based on the colour target (Figure 5-13), which define the landing pattern, where the UAS will land.

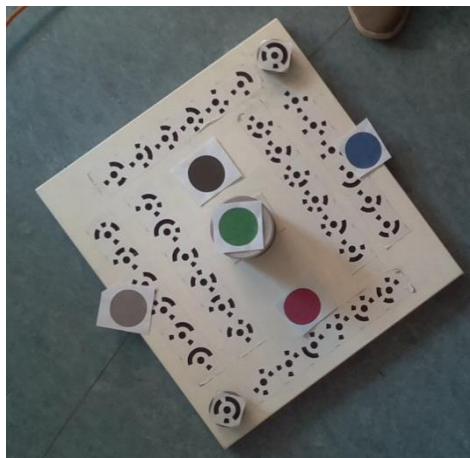


Figure 5-13. Coloured target on landing test field.

The landing pattern is composed by an aluminium plane, on which at least five circular targets were attached. In order to obtain high reliability and accuracy during the validation procedure, about 40 circular ring-coded target (Figure 5-9) were attached both on the plane face and on the three raised points.

5.6 Orientation

The camera orientation was computed by resection with respect to a landing frame. The resection was a linearization of collinearity Equations (5.2), in order to describe transformation of object coordinates (X, Y, Z) into corresponding image coordinates (x', y') .

$$\begin{aligned} x' &= x_0 + c \frac{r_{1,1}(X - X_0) + r_{1,2}(Y - Y_0) + r_{1,3}(Z - Z_0)}{r_{3,1}(X - X_0) + r_{3,2}(Y - Y_0) + r_{3,3}(Z - Z_0)} + \Delta x' \\ y' &= y_0 + c \frac{r_{2,1}(X - X_0) + r_{2,2}(Y - Y_0) + r_{2,3}(Z - Z_0)}{r_{3,1}(X - X_0) + r_{3,2}(Y - Y_0) + r_{3,3}(Z - Z_0)} + \Delta y' \end{aligned} \quad (5.2)$$

where the r_{ij} are the elements of a 3D rotation matrix \mathbf{R} :

$$\begin{bmatrix} x' \\ y' \\ c \end{bmatrix} = \mathbf{R} \begin{bmatrix} X - X_0 \\ Y - Y_0 \\ Z - Z_0 \end{bmatrix} \quad (5.3)$$

The image coordinates were function of the interior orientation parameters: $x_0, y_0, c, \Delta x', \Delta y'$; respectively: principal point coordinate, focal length and relative deviation due to distortion effects and exterior orientation parameters $(X_0, Y_0, Z_0, \omega, \phi, \kappa)$ of a camera. The first three were the position of the perspective center in object reference system, while the others were rotation angles: ω (tilt horizontal axis), ϕ (roll around azimuth axis), κ (roll around optical axes), as shown in Figure 5-14:

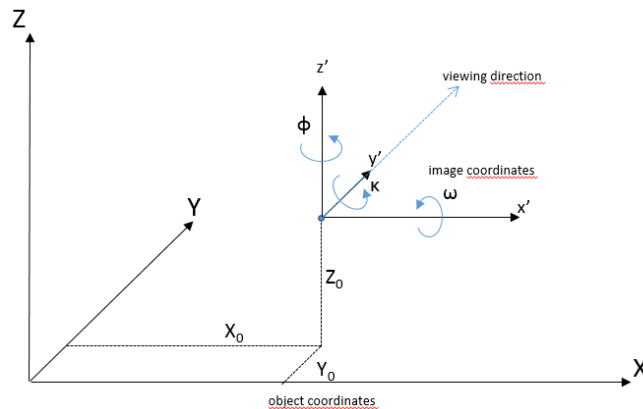


Figure 5-14. Two reference systems: the object SR (XYZ) and the camera SR (x', y', z') .

The collinearity equation system (5.1) can be rewritten in the following system of correction equations:

$$\begin{aligned} x' &= x_0' + vx' \\ y' &= y_0' + vy' \end{aligned} \quad (5.4)$$

where x_0' ; y_0' are the image coordinates computed using approximated orientation parameters, while vx' , vy' are the adjustment parameters to obtain the correct x' and y' image coordinates. The adjustment parameters can be obtained as linearization of the Equation (5.1), using as initial point the approximated orientation parameters employed to compute x_0' ; y_0' :

$$\begin{aligned} vx' &= \left(\frac{\partial x'}{\partial X_0} \right)_0 dX_0 + \left(\frac{\partial x'}{\partial Y_0} \right)_0 dY_0 + \left(\frac{\partial x'}{\partial Z_0} \right)_0 dZ_0 + \left(\frac{\partial x'}{\partial \omega} \right)_0 d\omega + \left(\frac{\partial x'}{\partial \varphi} \right)_0 d\varphi + \left(\frac{\partial x'}{\partial k} \right)_0 dk \\ vy' &= \left(\frac{\partial y'}{\partial X_0} \right)_0 dX_0 + \left(\frac{\partial y'}{\partial Y_0} \right)_0 dY_0 + \left(\frac{\partial y'}{\partial Z_0} \right)_0 dZ_0 + \left(\frac{\partial y'}{\partial \omega} \right)_0 d\omega + \left(\frac{\partial y'}{\partial \varphi} \right)_0 d\varphi + \left(\frac{\partial y'}{\partial k} \right)_0 dk \end{aligned} \quad (5.5)$$

Generally the approximated position of the camera does not provide good results, although they were corrected using a linearization procedure. Indeed the distance between the computed coordinates, using the abovementioned linearization procedure, and the measured coordinates approach to zero only after several iterations. At the end of the iterative process, the method is able to estimate the camera attitude and position (Luhman, 2011).

In order to solve the system in Equation (5.3) we need at least 3 points (not aligned), indeed such observations provide six equations, which allow estimating the six external orientation parameters. Of course, to increase the redundancy of the equation system (5.3), it is needed to add further observations, and a solution can be estimated using the classical least-square adjustment method.

5.7 Validation procedure

In order to inspect the accuracy and precision achievable employing the proposed methodology, a validation procedure was designed and then performed.

The aim of this validation procedure is to detect the potential accuracy and precision achievable. Therefore a comparison between Space Resection (SRM) and Bundle Adjustment Solution (BA) was carried out.

BA is well-known numeric method to compute a multi-images position using tie-points and ground control points; this technique assures high reliability and integrity on the solutions.

The validation procedure has been conducted following these four steps:

1. Designing and building of landing pattern, using two type of circular target: ring coded circular target and coloured circular target (section 5.5).
2. Photogrammetric survey of landing pattern following the classical procedure employed in close-range photogrammetry.
3. Camera positions and orientations by BA using all circular targets and by SRS using only coloured circular targets.
4. Comparison position and orientation for each camera, between BA and SRS results.

In this work the measurement of image coordinates targets are carried out employing two different methods:

- ✦ **LSM:** Least Square Matching is a powerful technique for all kinds of data matching problem. Here, its application to image matching was used through the software Photomodeler Scanner (Endoh et al., 2003). Due to the perspective angle, the circular targets present on the scene could be appear as ellipse on the image. The LSM is able to detect the correct center because it applies an affine transformation to recognize the shape correctly. Such approach achieve sub-pixel precision, and it is widely employed in industrial photogrammetry. Unfortunately, the LSM is not available in the OpenCV library.
- ✦ **CHT:** Circle Hough Transform is a feature extraction technique for detecting circles on images. This method is based on application of the Hough Transform (Hough 1962 and Duda et al. 1972) to edge map. The latter is obtained applying the Canny edge detector (Canny, 1986) with automatic thresholding on a single image. This approach is suitable for automatic recognition in soft real time, although the center of the circle is not always accurate due to the perspective angle of view, as previously described. Furthermore, it was already developed in the OpenCV library.

5.8 Comparison and Results

In order to compute the precision and accuracy achievable, it was fundamental to make a comparison.

The results obtained with the Bundle Adjustment procedure were more robust than the ones expected from the Space Resection Method, because the redundancy of the Bundle Adjustment was high and the network was well designed. In order to evaluate the results accuracy, the BA solution was taken as reference.

Thus, a comparison between the BA solution and the SRS one was carried out. The differences are reported in terms of mean, standard deviation and RMSE (Root Mean Square Errors) for each image acquired and considering two different methods of target detection: LSM and CHT. Firstly, a deep inspection about the photogrammetric survey is indispensable. The survey was carried out using 11 images taken at a distance of 1.5 meters and using 37 coded circular target. The obtained network is shown in Figure 5-15, which assures an average intersection angle of 67 degrees among all rays, furthermore each image is covered by at least 28 points.

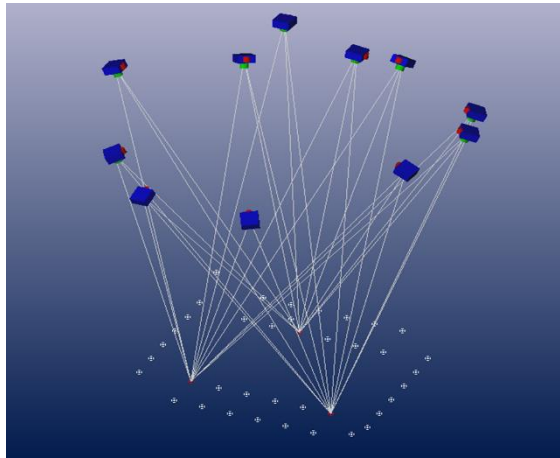


Figure 5-15. Camera network obtained.

The targets coordinates were estimated with high precision: indeed, the overall RMS vector length in 3D is 0.082 mm, while each camera precision values are reported in Table 5.2.

Table 5.2. Precision values about the camera position and camera attitude expressed in millimetres, after a BA procedure.

Name	Precision [mm]			Precision [degrees]		
	X	Y	Z	Omega	Phi	Kappa
C1	0.35	0.36	0.26	0.0239	0.0226	0.0092
C2	0.34	0.33	0.20	0.0236	0.0238	0.0086
C3	0.32	0.28	0.22	0.0212	0.0197	0.0099
C4	0.32	0.35	0.21	0.0250	0.0214	0.0090
C5	0.27	0.28	0.19	0.0219	0.0197	0.0087
C6	0.26	0.32	0.24	0.0235	0.0203	0.0098
C7	0.24	0.32	0.27	0.0230	0.0186	0.0110
C8	0.22	0.25	0.26	0.0211	0.0165	0.0120
C9	0.28	0.24	0.26	0.0190	0.0170	0.0110
C10	0.34	0.38	0.26	0.0250	0.0222	0.0105
C11	0.30	0.34	0.23	0.0231	0.0223	0.0086
C12	0.32	0.32	0.20	0.0231	0.0232	0.0090
C13	1.61	1.60	0.32	0.0584	0.0584	0.0092
C14	1.21	1.19	0.21	0.0504	0.0510	0.0090

The solution provided by the Bundle Adjustment procedure was quite precise and robust, therefore a comparison with SRS solution was performed.

Two different approaches were carried out, in both cases only 5 circular targets were considered. A first approach was executed using the LSM to determine the image coordinates of the targets, whereas the second approach was performed using the CHT method for target detection. The first one provides goods results almost in every images, especially when the image is very tilted, because it is able to determine the correct target center even if the circular target appears on the image as an ellipse.

The comparison among the BA solution and both SRS solution is described in Table 5.2, Table 5.3 and Figure 5-16, where are reported the absolute differences in 3D space of cameras position, and the angle differences.

Table 5.3. Position and attitude after LSM procedure.

Name	LSM detection			
	Omega [deg]	Phi [deg]	Kappa [deg]	3D [mm]
C1	0.002	-0.014	-0.034	0.24
C2	-0.046	0.116	0.023	1.96
C3	0.080	0.052	0.029	1.70
C4	0.020	-0.034	-0.009	0.75
C5	0.009	0.110	0.014	1.57
C6	0.124	-0.124	0.064	2.71
C7	0.046	-0.037	-0.032	1.05
C8	-0.059	-0.102	0.008	2.08
C9	-0.321	-0.083	-0.004	5.16
C10	-0.027	0.077	0.009	1.25
C11	0.026	0.016	0.045	0.55
C12	-0.157	-0.134	-0.057	10.69
C13	-0.008	0.046	0.082	1.31
C14	-0.032	0.084	0.061	2.11

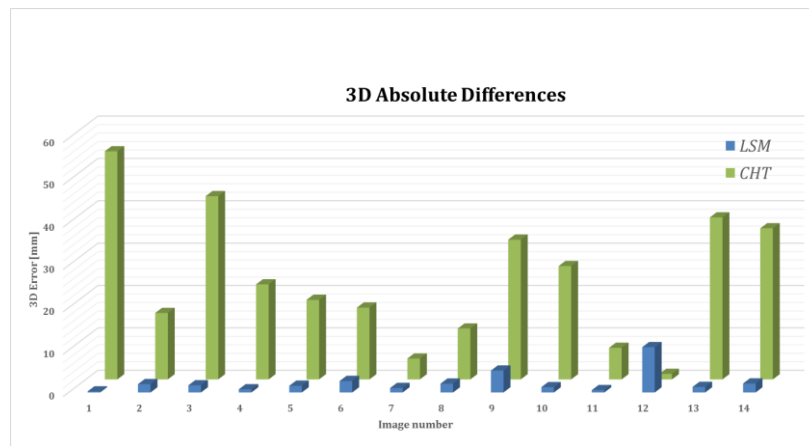


Figure 5-16. Error differences between LSM and CHT.

The histogram depicted in Figure 5-16 shows the differences among the 3D position of perspective center computed by BA and SRS. Specifically, in green the differences using the HGH approach are reported, while in blue LSM.

5.9 Conclusions

In this section a novel vision navigation system was done, in order to make attitude and position corrections through real time data (frames) and to aid the UAS during the landing procedure.

The SRS and BS algorithms was previously developed by S. Del Pizzo et al.; so in this Ph.D. work the goal was to develop and test the electronic platform (camera and ground station) and the HGH algorithms (in OpenCV).

6. UAS Endurance Enhancement

6.1 Introduction

Most civilian uses of UASs require the air vehicle to fly at speeds lower than 50 kts (70 km/h) and at low heights, and many applications need the ability of the aircraft to hover (e.g. power line inspection, subsurface geology, mineral resource analysis, or incident control by police and fire services) (Chapter 1). Moreover, in some cases this type of platform needs to execute extended missions with significant flight duration time. Increasing endurance generally comes at a cost in terms of fuel consumption and airframe complexity, resulting in reduced efficiency of payload and/or range for size, mass and financial cost.

This chapter focuses on the flight time of the vehicle, and proposes an alternative approach to improve endurance of a non-expensive, commercial quad-rotor, by applying a balloon to reduce weight and power consumption needed for flight. The small quad-rotor Conrad Quadcopter 450 ARF (Appendix A) has been equipped with a payload composed by: a Global Positioning System (GPS) receiver module, an Inertial Measurement Unit (IMU), a sonar altimeter, a small camera module and main microcontroller hardware (Arduino, Raspberry). Typical endurance is less than 2 hours (without any payload) (Wang et al., 2013), whereas in our case (motor propeller plus the payload) the flight time has found to be less than 1 hour.



Figure 6-1. Conrad 450 (ArF) 35 MHz.

Balloons are not so often utilized, because they are not easily maneuverable, but a hybrid solution (quad-rotor merging) could effectively exploit the advantages of a quad-rotor vehicle (flexibility, well-designed structure, security) and the strength points of a balloon (low noise,

low energy consumption, buoyancy providing most of the flight lift, increasing endurance by reducing power consumption) (Carson et al., 1971). The most interesting improvement created by such an HUAS (Hybrid Unmanned Aircraft System) is the static lift provided by the balloon, which, combined with the fan lift of the propulsion system, allows the vehicle to achieve easy takeoff, climbing, hovering and landing with reduced power usage. The basic quantities to be determined for a preliminary design of this hybrid vehicle are: weights, gross static lifting capability of the balloon (i.e., the portion of the balloon's total lift attributable to its buoyancy), lifting gas properties, atmospheric conditions in the flight range, and influence of the balloon size on lift.

Although the dynamics and aerodynamics of the HUAS operations must be considered in a complete design of the balloon, we will consider only the balloon static performance, following the approach described in (Barton, 2008).

The following nomenclature is adopted for the following sections:

L = static lift;

W = weight;

ρ_g, ρ_{air} = gas density, air density;

V_g = gas volume;

g = gravitational acceleration (9.8066 ms^{-2});

p = pressure;

p_g, p_{air} = gas pressure, air pressure;

R = perfect gas constant ($8.314 \text{ Pa m}^3 \text{ mol}^{-1} \text{ K}^{-1}$)

T_g, T_{air} = gas temperature, air temperature.

6.2 HUAS Conceptual Design

A stand-alone balloon is not easily maneuverable mainly for its big inertia, but in static conditions it is reliable. Considering a conventional quad-rotor coupled with a balloon, it is possible to manage and control the balloon by means of propeller speed changes. The idea exploited is to adapt a balloon to the chosen quad-rotor, creating hybrid lift (static lift and fan lift) to achieve takeoff, hovering and landing with reduced energy consumption, thus improving the flight time (endurance). The overall system is able to correct any change of flight attitude due to voluntary actions or instability induced by the balloon. Thrust propellers improve maneuverability of the HUAS. A simple web frame is chosen to wrap the balloon and link to

quad-rotor. The web frame is a non-rigid solution, adopted to have the two linked but independent systems, each with its own function; the balloon for static gross lift (mainly upward) and the quad-rotor for flight control. The buoyancy of the balloon is able to provide most of the flight lift, therefore reducing power consumption of the quad-rotor and increasing flight endurance and usage of the craft for longer missions.

A 3D CAD software was used to make a preliminary structure for successive balloon size validation. Figure 6-2 and Figure 6-3 show the structure of the HUAS, with a basic balloon, support lines, safety lines and a synthetic model of the quad-rotor. The balloon diameter has been chosen to be 1.5 m.

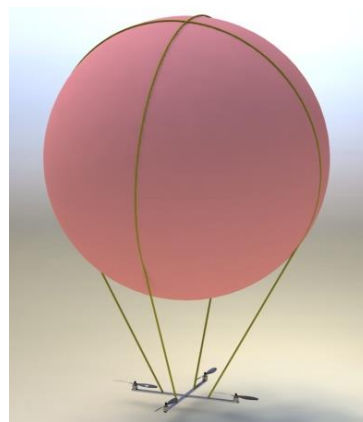


Figure 6-2. HUAS preliminary concept.

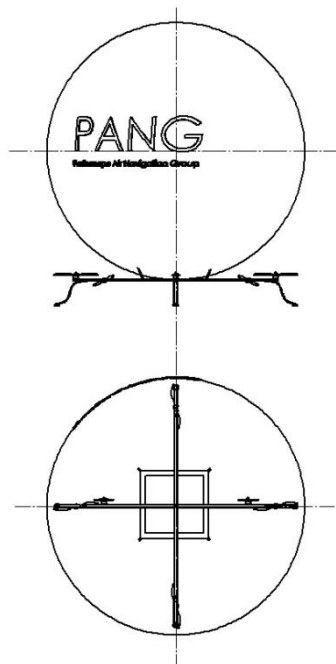


Figure 6-3. HUAS CAD 2D.

The installed battery packs are lightweight LiPo (Lithium Polymer), with capacities of 1800mAh and 4000mAh @11.1V respectively (Figure 6-4).



Figure 6-4. LiPo batteries used during tests.

Endurance in minutes, without the balloon, for a normal mission (take-off, hovering and landing) is shown in Table 6.1.

Table 6.1. Endurance for the LiPo batteries previously considered.

Capacity of LiPo battery	Take-off and landing	Hovering
4000 mAh	< 5 min	≈ 40 min
1800 mAh	< 5 min	≈ 15 min

The next section focuses on HUAS weight estimation and balloon sizing. Each configuration was checked through a static analysis in CAD software, eventually choosing an optimal configuration achieving a good weight/lift compromise.

6.3 Weights Estimation and balloon sizing

The analytical techniques described in (Barton, 2008) were applied, considering three subsystems of the HUAS:

- ✦ inflation gas;
- ✦ balloon structure;
- ✦ quad-rotor system.

The weights and the static performance of each parts were determined separately and successively summed. In this conceptual design phase, inertia and dynamic properties were not considered, postponing their evaluation in future work.

6.4 Take-off Weight Estimation

For a correct evaluation of the gross static lift provided by the balloon, it was necessary to estimate the gross take-off weight (W_{TO}) of the HUAV, a quantity which depends on all the components of the HUAV (the quad-rotor structure, payloads (sensors on board), battery pack, support lines, safety lines, tether lines, the balloon itself).

The net force acting on the balloon tether line equals the gross static lift of the balloon minus the constant tare of the bag. Equation (6.1) gives the gross static lift of the balloon (Barton, 2008):

$$L = (\rho_{air} - \rho_g)V_g \quad (6.1)$$

where V_g is the volume occupied by gas when the balloon is fully inflated. In ideal conditions, the gross lift is equal to W_{TO} , given by:

$$W_{TO} = W_{eq} + W_B + W_{batt} + W_p \quad (6.2)$$

where weights are referred to: empty quad-rotor W_{eq} , balloon (lines, gas and bag included) W_B , battery pack W_{batt} , payload (sensors onboard) W_p . Obviously, W_B depends on the balloon size, and is the unknown parameter, whereas the other contributions to W_{TO} are constant and known.

Using a weight coefficient $k_x = W_x/W_{TO}$ (with x representing any of the subscripts in Equation (6.2)), Equation (6.2) can be rewritten as:

$$k_{eq} + \frac{W_B}{W_{TO}} + k_{batt} + k_p = 1 \quad (6.3)$$

Moreover, we derive W_{TO} as follows:

$$W_{TO} = -W_B / (k_{eq} + k_{batt} + k_p) \quad (6.4)$$

The UAV system considered in this work has a total weight ($W_{eq} + W_{batt} + W_p$) of about 3 kg: this was, according to Archimedes' law, the buoyancy requirement.

6.5 Balloon Static Performance and Sizing

A classical airship has various configurations: flabby balloon with ballonnet (air chamber), partially inflated, fully inflated (Figure 6-5. Balloon configurations.). It also can be composed of two components: a hull and a tail fin assembly. In this study, a fully inflated configuration (logging balloon, without tail fin) was chosen.

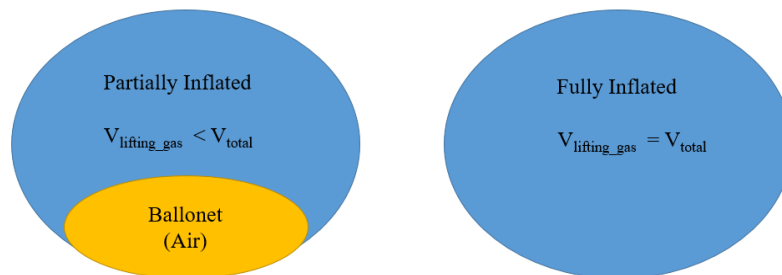


Figure 6-5. Balloon configurations.

For safer flight conditions, the volume of gas in the fully inflated configuration must always be less than or equal to the total volume. The correct sizing must also consider temperature and pressure influences on the lifting gas. The lifting gas required to create buoyancy must obviously have density less than the air density. Among several available types of lifting gases (hot air, hydrogen, helium, ammonia, etc.), we chose helium (He), because it is easily available

and ready to use without many control systems (valve, pipes, etc.). A comparison of helium vs. hydrogen was shown in Table 6.2.

Table 6.2. Lift comparison considering various gases.

Lifting gas	Density at sea level and 0°C	Lifting force of 1m³ of gas
Helium (He)	0.178 kg/m ³	11.8 N
Hydrogen (H)	0.090 kg/m ³	10.9 N
Air	1.292 kg/m ³	##

From Equation (6.1), we considered a lifting force for 1 m³ of gas at sea level (SL) and 0 °C. Lift decreases proportionally with the altitude (temperature and pressure). Lifting force calculation does not include the bag and lines of the balloon; it was only referred to 1 m³ of lifting gas.

The balloon was modeled as a sphere, which contains a sufficient lifting gas that can equalize, or almost, W_{TO} . The main mission parameters to be defined were: altitude (pressure altitude¹ – PA , temperature T), gas density, and air density. This work considers a typical PA in the range 6-20 m (20-65 ft) and air temperature of 290 K (17 °C), reasonably constant in the selected altitude range. The density-pressure-temperature nomogram (Figure 6-6) can be used to determine the inflation requirements of the balloon.

¹ Pressure altitude is the reading of an altimeter when adjusted to the standard MSL (mean sea level) atmospheric pressure of 1013.25 mbar (29.98 inches of mercury). It does not correspond to the actual elevation.

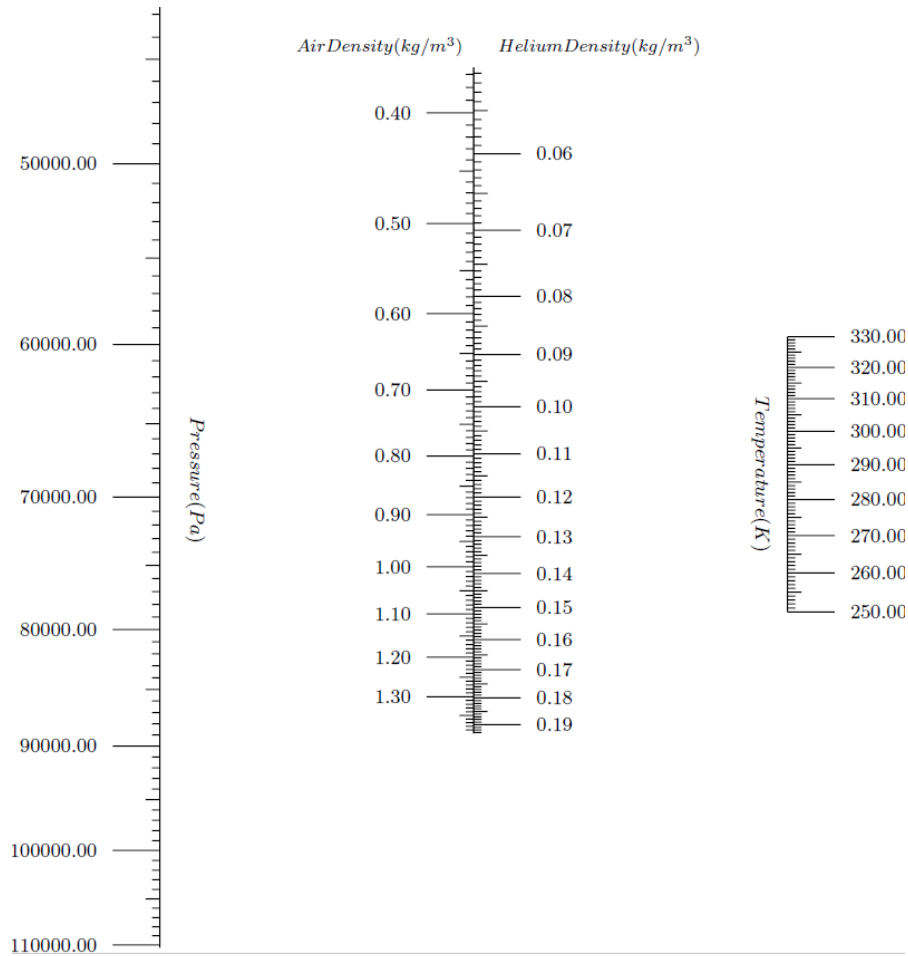


Figure 6-6. Nomogram for initial inflation.

The blue dashed line (Figure 6-7) shows our conditions, and determines a balloon gas density of 0.168 kg/m^3 . The design volume V_D of the spherical balloon and the weight of the inflation gas, W_{He} , were computed through use of the perfect gas law, giving:

$$V_D = \frac{W_{T0}}{\left(1 - \frac{p_g}{p_{air}} \frac{R_{air}}{R_g}\right) \frac{g p_{air}}{R_{air} T^*}} \quad (6.5)$$

$$W_{He} = \rho_g V_D \quad (6.6)$$

where $T^* = T_g / T_{air}$ and V_D refers to a fully inflated balloon.

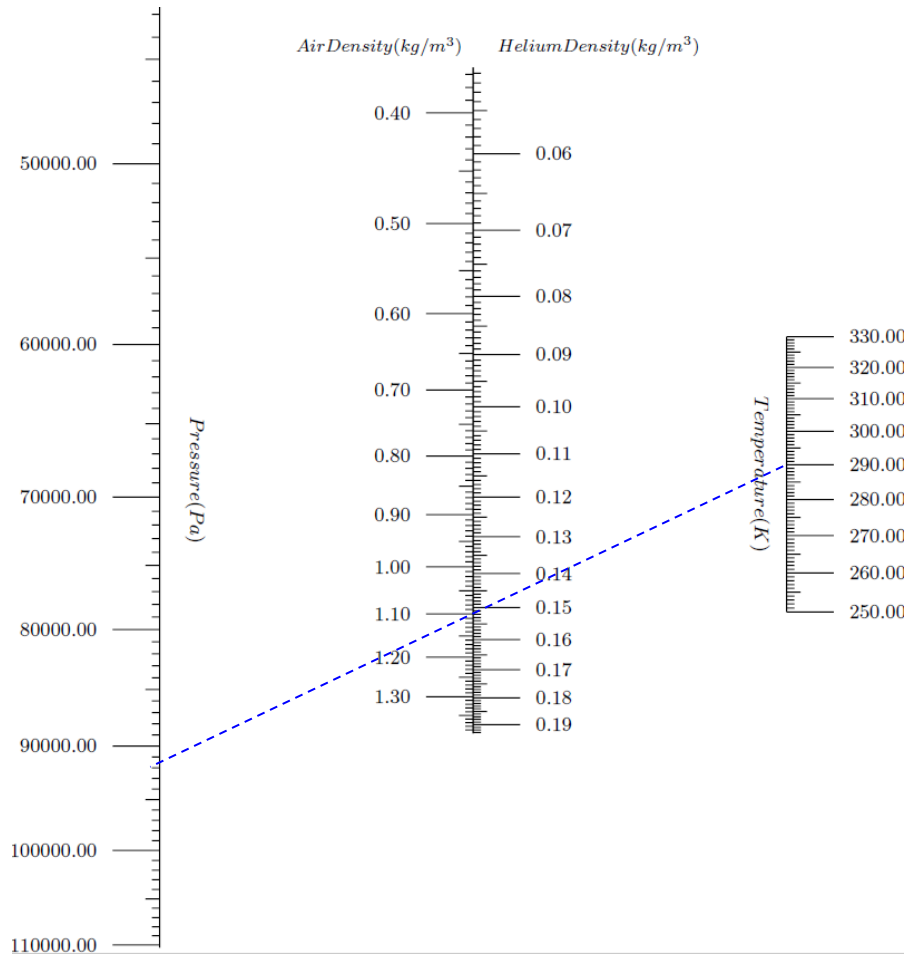


Figure 6-7. Initial inflation in operative flight condition.

The Equation (6.7) gives the design volume (cubic feet are the preferred unit in the compressed-gas industry) required in standard conditions, V_{STD} :

$$V_{STD} = \frac{\rho_g}{\rho_{STD}} \frac{W_{TO}}{\left(1 - \frac{p_g}{p_{air}} \frac{R_{air}}{R_g}\right) \frac{g p_{air}}{R_e T^*}} \quad (6.7)$$

Successively, it was possible to calculate the expected gross static lift, considering the nomogram for initial inflation (Figure 6-8).

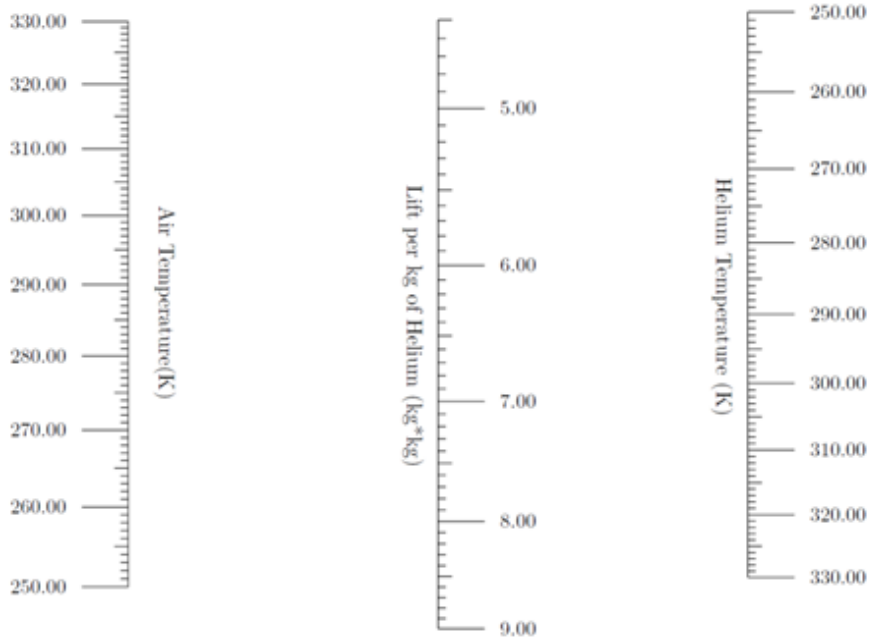


Figure 6-8. Nomogram for expected gross static lift.

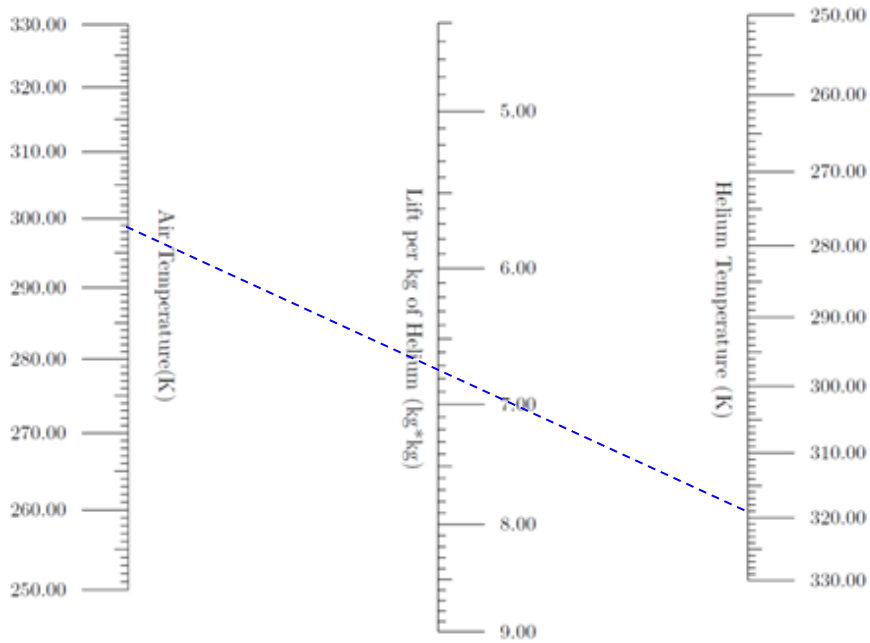


Figure 6-9. Nomogram for expected gross static lift ($T_{air}=299$ K, $T_{He}=322$ K).

For this application the expected gross static lift (L_{exp}), from Figure 6-9 (blue dashed line), was 6.78 kg of lift per kg of He, considering the maximum expected temperatures: $T_{air}= 299$ K (≈ 27 °C) and $T_{He}= 322$ K (≈ 49 °C).

The gross static lift is given by:

$$L = \frac{L_{\text{exp}} \rho_g W_{TO}}{\left(1 - \frac{p_g}{p_{\text{air}}} \frac{R_{\text{air}}}{R_g}\right) \frac{\rho_{STD} g p_{\text{air}}}{R_{\text{air}} T^*}} \quad (6.8)$$

Generally, L depends on the atmospheric pressure and temperature, but we considered a constant pressure value, due to the low altitude and the small altitude range chosen. The design volume V_D was the main parameter that determines gross static lift for a specific diameter of the balloon. Various diameters have been considered, in order to attain good efficiency ($L(V_D)/\text{Drag} \approx 1$), at low altitude and low speed.

Recalling that W_{TO} is equal to 3 kg, the balloon weight W_B , given by:

$$W_B = W_{He} + W_{bag} + W_{lines} \quad (6.9)$$

is to be added, whereas W_{He} is given by Equation (6.6), and the remaining weights are a function of V_D and the material used for the bag and the lines. We will show in the next section a set of diameters and the corresponding solutions.

The balloon thickness was obviously dependent on the helium pressure, which in turn depends on temperature, volume of the bag (V_D) and number of moles of He. Using the ideal gas law and assuming operational conditions at $T = 17 \text{ }^\circ\text{C}$ (290.15 K) and $p = 1031.25 \text{ hPa}$, the helium pressure, which must be sustained by the structure (bag), was given by:

$$p_{He} = \frac{nRT}{V_D} \quad (6.10)$$

The Young-Laplace law (Batchelor, 2000) can be used to derive the pressure difference $\Delta p = p_{He} - p_{air}$, across the interface between air and helium, assuming a spherical balloon of radius r :

$$\Delta p = \frac{2\tau(r)}{r} \quad (6.11)$$

where τ was the surface tension (obviously, Δp should be less than the maximum tension of the balloon, to avoid bursting). The material chosen for the balloon was PVC (Polyvinyl chloride), whose mechanical characteristics were summarized in Table 6.3.

Table 6.3. PVC mechanical characteristics.

Property	Units	Method	Value
Specific weight	g/cm ³	ISO 1183	1.42
Yielding tension	MPa	DIN EN ISO 527	58
Elastic modulus	MPa	DIN EN ISO 527	3000
Hardness SHORE D	-	ISO 868	82

It turned out that the tension forces τ are small and the balloon pressure was very close to the atmospheric pressure. Therefore, thickness in the range 0.10-0.30 mm was sufficient to guarantee the necessary lift without reaching bursting conditions.

6.6 Preliminary Results

Table 6.4 summarizes the expected operating conditions.

Table 6.4. Operating conditions.

Pressure Altitude [m]	Air or Helium Temperature [° C]	Helium expected gross static lift [kg per kg of He]	Helium density [kg/m ³]	Air density [kg/m ³]
7	17.1045	2.84	0.1681	1.2241
10	17.0850	2.84	0.1681	1.2238
13	17.0655	2.84	0.1681	1.2234
16	17.0460	2.84	0.1682	1.2231
19	17.0265	2.84	0.1682	1.2227

The density and expected gross static lift were quite similar (see Figure 6-8 and Figure 6-9) and considered constant. On average, we have a gross static lift of 2.84 kg per one kilogram of helium. In this case, one kg He was sufficient to lift the UAS and sensors ($W_{eq} + W_{batt} + W_p$). Using a spherical configuration, the total gross static lift becomes a function of the balloon diameter, as shown in Figure 6-10 (see also Equation 6.6).

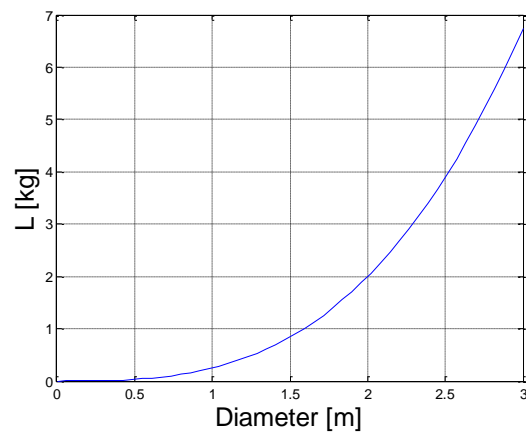


Figure 6-10. Gross static lift vs. balloon diameter.

Figure 6-11 shows the dependence of the gas weight, to be added to obtain W_{TO} , on the balloon diameter.

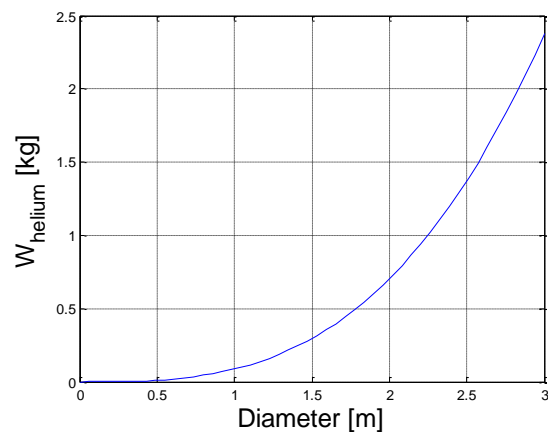


Figure 6-11. Gas weight vs. balloon diameter.

The total balloon weight W_B was estimated considering a PVC bag with thickness in the range 0.18-0.28 mm. The weight for link lines is practically constant.

A diameter of 2.7 meters provided full W_{TO} equalization (bag and lines included), but in terms of control and manoeuvring it was a poor choice, since such a value involves a big drag force, and therefore weak manoeuvrability and control. Drag refers to the forces acting opposite to the relative motion of any object moving with respect to a surrounding fluid; it depends on body (cross sectional area).

Since our aim was to reduce power consumption of the rotors to increase endurance, it was not necessary to maximize total gross lift (i.e. $L = W_{TO}$). In this preliminary design, a solution with

gross static lift less than W_{TO} has been chosen, to ensure low diameter, low drag force, good manoeuvrability and control (Figure 6-12).

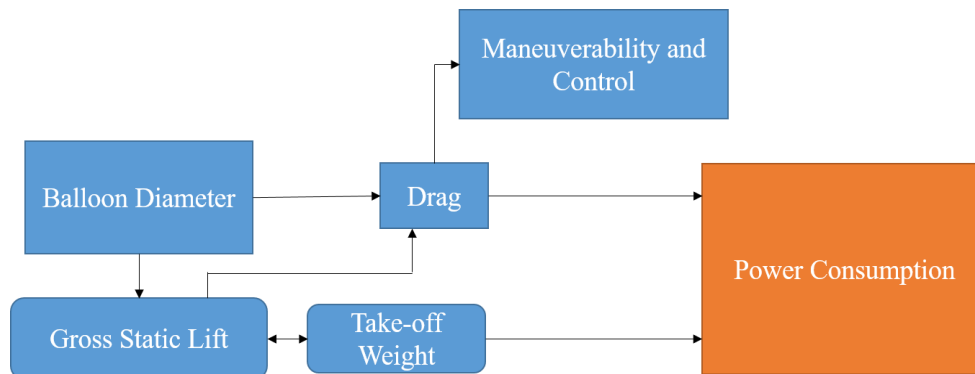


Figure 6-12. Relationship among design parameters.

Under these hypotheses, considering initial inflation parameters, it will be possible to estimate gross static lift values for a specific balloon diameter. The gross lift generated was about 67% of W_{TO} , for a balloon diameter of 2 meters: in this condition the HUAS returns to the ground by its own gravity. During landing and hovering, the lift provided by the balloon and quad-rotor can help it to get hovering height; so, the total lift was less than the HUAS weight (sensors included). If the propeller speed decreases, HUAS can land, due to its own weight.

Table 6.5 shows increased performance of the HUAS in the hovering phase, with respect to the standard (i.e. without balloon) quad-rotor.

Table 6.5. HUAS vs. UAS endurance.

	UAV		HUAV	
	Take-off and Landing	Hovering	Take-off and Landing	Hovering
4000mAh	< 5 min	≈ 40min	< 5 min	≈ 60min
1800mAh	< 5 min	≈ 15 min	< 5 min	≈ 25min

6.7 Conclusions

This last section presented a conceptual design of a hybrid-electric UAS (quad-rotor + airship), demonstrating the feasibility of an extended cruise endurance, focusing on the design drivers affecting the craft flight time. In electric-motor/battery powered UAS designs, increasing

endurance requires heavier batteries, with a consequent increment of weight of the UAS. The alternative approach presented in this work increases endurance by using a balloon, which optimizes the ratio endurance/weight. It was advisable to keep this ratio as low as possible.

Installation of a balloon, with a diameter of about 2 meters, gives a significant increase in flight time, as demonstrated in test missions developed *in situ* (in urban traffic monitoring). As shown in Table 6.5, the HUAS endurance (with 1800-mAh LiPo battery) increased by +80%.

Further investigations will focus on stability and control problems (Barton, 2008) of the HUAS, caused by wind flow (e.g. vertical/horizontal gusts) and pendulum effects during left/right turning, which make trajectory tracking and attitude stabilization challenging tasks. These effects mainly depends on nonlinearities like coupling between the quad-rotor and the balloon. Non-linear techniques (Fantoni & Lozano, 2002) are currently under study, together with a structural modification of the craft. The foreseen installation of two additional propellers (Figure 6-13) will provide thrust for flight direction changing. To remove the non-linearity introduced by pendulum moments, the tether lines will be reduced, obtaining a final UAS + balloon single structure shown in Figure 6-14. Preliminary simulations and dynamic studies confirmed improved stability of the HUAS, allowing us to tune the mechanical design for optimal control sensitivity and disturbance rejection.

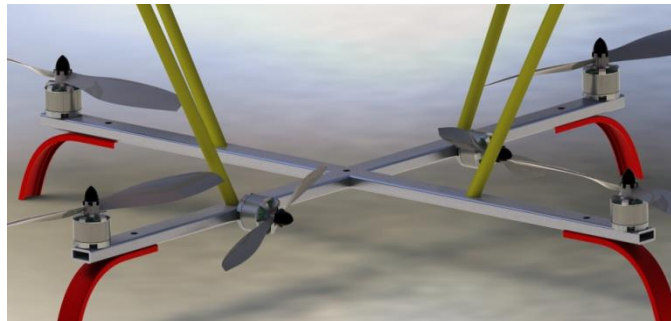


Figure 6-13. Latest HUAS configuration, with directional propellers.

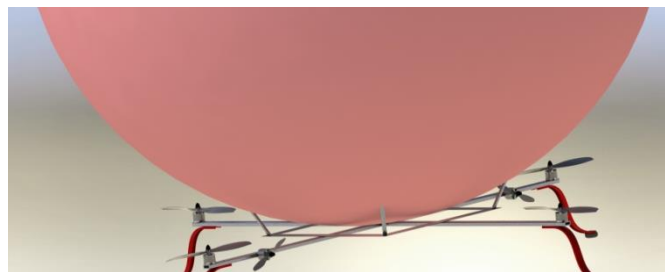


Figure 6-14. Newest configuration for non-linearity reduction.

Another issue was the purity of the lifting gas (it is not easy to find 100% pure He), which could impair the gas performance during the mission. The impact of non-pure helium on the lifting properties is currently under examination.

7. Conclusions

This Ph.D. thesis wants to be a novelty contribution to the many topics covered in the UASs applications. A monitoring and control landing system was done, in order to assist the remote pilot during the landing procedure when the environmental condition are adverse. The whole system was composed by Ultrasonic Sensor, Infrared Sensor and Optical Sensor; each one of them has been discussed in the Chapters of this work.

According to Joint Publication 1-02, DoD Dictionary (OSD, 2002), I wish to conclude this work by giving the definition of UAS or unmanned aircraft UA:

“A powered aerial vehicle that does not carry a human operator uses aerodynamic forces to provide vehicle lift, can fly autonomously or be piloted remotely, can be expendable or recoverable, and can carry a lethal or non-lethal payload. Ballistic or semi ballistic vehicles, cruise missiles, and artillery projectiles are not considered unmanned aerial vehicles.”

8. Appendix A

UAVs Features

This appendix describes the main features of the UASs utilized in this Ph.D. thesis.

8.1 Conrad 450 ArF

The research conducted in Chapter 2, 5 and 6 used as a test bed this quad-rotor (CONRAD, 2016), made from Reely and distributed over Conrad. The central control is based on an efficient (Atmel-Mega 128) microprocessor, which conveys the control commands to the processors for the motor electronics via a bus system.

A complex control electronics comprising of position and acceleration sensors as well as efficient RISC microprocessors stabilize the quad-rotor during flight.

Highlights and details were listed below:

- ✦ Flying platform for air reception;
- ✦ Up to 500 g additional loads possible;
- ✦ System driven Microprocessor;
- ✦ Individual programming by optional software;
- ✦ Ideally suitable for night flight.





Figure 8-1. Photos of 450 ArF quad-rotor.

Table 8.1. 450 ArF main dimensions (CONRAD, 2006).

Dimensions (Ø x H)	450 mm x 165 mm
Main rotor Ø	260 mm
Weight	670 g
Load Capacity	~ 500 g

8.2 RC EYE NovaX 350

This UAS (RC Logger NovaX, 2015) consolidates rigid design, modern aeronautic technology as well as easy maintainability into one outstanding versatile multi-rotor platform. In the professional field, UAV are used for the most different tasks (aero photogrammetry, search and rescue, environment monitoring, industrial component inspection, etc.). It is also possible to choose a fixed-wing UAS configuration, but the airspace is typically limited. A fixed-wing configuration needs a runway to land and take off, so rotorcraft are much flexible in these procedures.

The NovaX 350 is fully electric, with four propellers installed on direct current brushless motor in connection with a specially developed control, user programmable.

The NovaX 350 design is depicted in Figure 8-2:

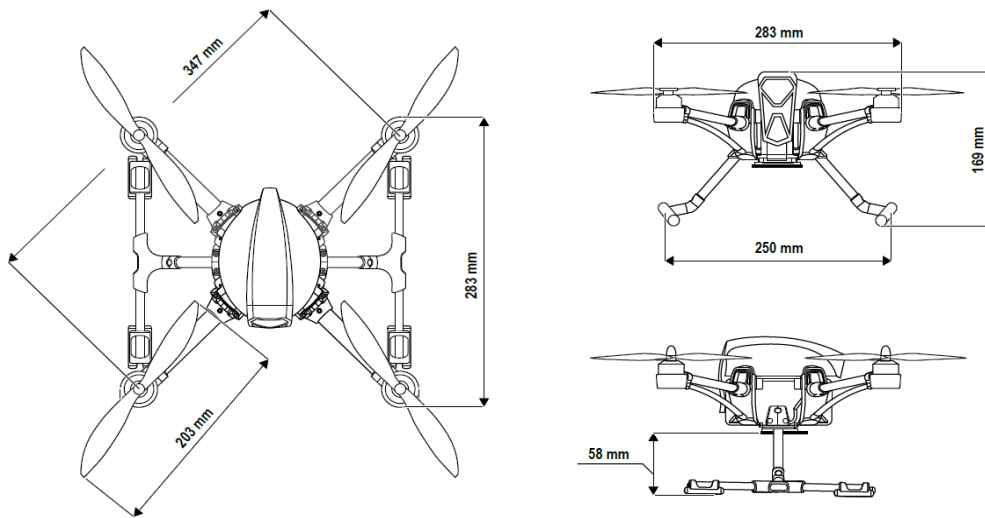


Figure 8-2. RC NovaX 350.

This vehicle can be operated both indoors and outdoors during calm weather conditions (without wind). Is preferred, for be in safe, to do outdoor analysis. The built-in electronic controls can balance out small undesired changes to the flight altitude. Aim is to control and manage this system (in particular landing procedure, and flight mechanics main parameters), through IR+SR sensors distance acquisition.

The RC EYE NovaX 350, is classified like a small/mini UAS, according to Table 1.1 and Table 1.3 (OSD, 2001).

The sensors available during the navigation depends on the flight mode and are described in table below:

Table 8.2. Activated sensors.

Sensor	Application	Flight Mode		
		Basic	Altitude	GPS
Gyroscope	Orientation	●	●	●
Accelerometer	Leveling	●	●	●
Barometer (Atmosphere Pressure Sensor)	Altitude	-	●	●
GNSS sensor	GPS	-	-	●

8.3 RC EYE One Xtreme

The RC Eye One Xtreme (Figure 8-3. RC EYE One Xtream.Figure 8-3), a micro quad-rotor, is a vehicle of a new series (Nonami et al., 2010; RC Logger Eye, 2015). In this case, the UAS is smaller than X5C, but better in terms of performance. Micro quad-rotors will be the future of UAS technologies.

The platform accommodates the latest 6-axis gyro stabilization technology, outstanding brushless motor (better than X5C DC motors) driven flight control, all embedded within a robust yet stylish frame design. The sturdy lightweight construction is an ideal platform for flight applications ranging from aerial surveillance, imaging or simply unleashing acrobatic fun flight excitement. It is possible to select two flight modes: beginners and experts flight enjoyment alike. In this work, for data session, beginner's mode is enabled.

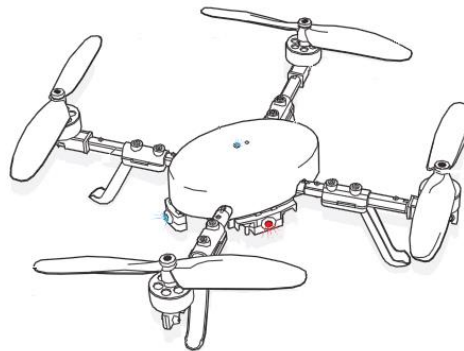


Figure 8-3. RC EYE One Xtream.

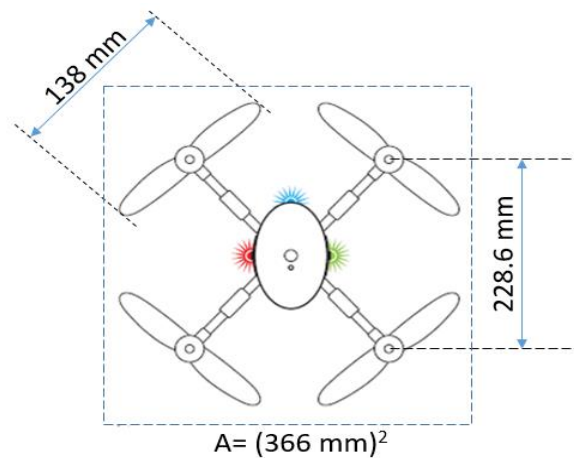


Figure 8-4. RC Eye One Xtreme main dimensions.

A 2.4-GHz receiver equips quad-rotor, therefore it is possible to configure a 2.4-GHz transmitter, in order to control and manage it. As well as X5C, also RC Eye One Xtreme is fixed on a tripod during data collection.

Both UASs use different colors (e.g. for propellers, led, legs, etc.) to distinguish the nose from the tail, this is important for the referencing during data collection. Each point acquired, need to be referenced respect a reference coordinate system. Both UAS data collection and measurements was evaluated in a reference system, where its origin is the centroid of the vehicle.

References

- 3DRAG, (2016) *Product Description*, <https://store.open-electronics.org/3Drag%203D%20printer%20KIT>. [accessed, January, 13, 2016].
- Austin, R., (2010). *Unmanned Aircraft Systems – UAVs Design, Development and Deployment*. John Wiley & Sons, Ltd, Publication, Vol. 54.
- Arduino.cc, (2016) <https://www.arduino.cc/en/Main/ArduinoBoardMega2560#techspecs>. [accessed July, 13, 2016].
- Barton, S.A., (2008). Stability Analysis of an Inflatable Vacuum Chamber. *Journal of Applied Mechanics*, Vol.75, Issue 4.
- Batchelor, G.K., (2000). *An Introduction to Fluid Dynamics*. Cambridge University Press.
- CONRAD, <http://www.conrad.com/ce/en/product/208000/QUADROCOPTER-450-ARF-35-MHz>, [accessed January, 15, 2016]
- Climatic Chamber KK-105, (2016). *Technical Datasheet*, <http://www.kambicmetrology.com/climatic-chambers/kk105-ch>, Kambic Ltd. [accessed July, 20, 2016]
- Canny, J.A., (1986). A computational approach to edge detection. *IEEE Transaction Pattern Analytic Machine Intelligence*, Vol. 8, no. 6, pp. 679-714.
- Carson et al., 1971 - Carson, W.W., & Peters, P.A., (1971). Gross Static Lifting Capacity of Logging Balloons. Pacific Northwest Forest and Range Experiment Station. Forest Service, US Dept. of Agriculture, Vol. 152.
- Dickerson, L., (2007). UAVs on the rise. *Aviation Week & Space Technology*, Aerospace Source Book 2007, Vol. 166, no. 3.
- Dean, E. A., (1979). Atmospheric Effects on the Speed of Sound. Technical Report of Defense Technical Information Center, Battelle Columbus Labs Durham NC.
- Duda et al., 1972 - Duda, R.A., & Hart, P.E., (1972). Use of the Hough transformation to detect lines and curves in pictures. *Communications of the ACM*, Vol. 15, no. 1, pp. 11-15.
- DHT11 sensor, (2010). D-robotics, *Technical Datasheet*, www.micropik.com/PDF/dht11.pdf, www.droboticonline.com. [accessed July, 21, 2010]
- Diosi et al. 2005 - Diosi, A., Geoffrey T., & Lindsay K., (2005). Interactive SLAM using laser and advanced sonar. Proceedings of the 2005 IEEE International Conference on Robotics and Automation. IEEE, pp. 1103-1108.
- Eisenbeiss, H., (2004). A Mini Unmanned Aerial Vehicle (UAV): System Overview and Image Acquisition. *2004 International Workshop on "Processing and Visualization using High-Resolution Imagery"*. Institute for Geodesy and Photogrammetry, ETH- Hoenggerberg, Zurich, CH.
- Endoh et al., 2003 - Endoh, N., Tsuchiya, T., & Yamada, Y. (2003). Relation between received pulse of aerial ultrasonic sonar and temperature and relative humidity. *World Congress on Ultrasonic*, Paris.
- Farid bin Misan et al., 2012 - Farid bin Misnan, M., Arshad, N.M., & Razak, N.A., (2012). Construction sonar sensor model of low altitude field mapping sensors for application on UAV. *IEEE 8th Colloquium on Signal Processing and its Applications*, IEEE, pp. 446-450.
- Faugeras, O., (1993). *Three dimensional computer vision: a geometric viewpoint*, MIT press.
- Fantoni & Lozano, 2002 - Fantoni, I., & Lozano, R., (2002). *Non-linear Control for Underactuated Mechanical Systems*, Springer Science & Business Media, London, UK.
- Gelb, A., (1974). *Applied Optimal Estimation*, Cambridge, MIT Press, MA, USA.

- Graham, G. (2006). The Standard Atmosphere. A mathematical model of the 1976 U.S. Standard Atmosphere.
- HC-SR04, (2010). Ultrasonic ranging module, *Technical datasheet*, ITead Studio.
- HD2817T, (2011). Manual, Delta Ohm HD281T, Transmitter, indicator, ON/OFF regulator, temperature and humidity datalogger. Rev. 1.2, November, 28th, 2011.
- Hough, P.V.C., (1962). Method and means for recognizing complex patterns. Patent, US3069 654, USA.
- Luhman et al., 2011 - Luhman, T., Robson, S. Kyle, S., & Harley, I., (2011). *Close Range Photogrammetry, principles techniques and applications*, Whittles Pub.
- Ludington et al., 2007 - Ludington, B., Johnson, E.N., & Vachtsevanos, G.J., (2007). Vision Based Navigation and Target Tracking for Unmanned Aerial Vehicles. *Advances in Unmanned Aerial Vehicles – State of Art and the Road to Autonomy*, Springer Netherlands, pp. 245-266.
- Mustapha et al., 2012 - Mustapha, B., Zayegh, A., & Begg, R. K., (2012). Multiple Sensors Based Obstacle Detection System. *4th International Conference on Intelligent and Advanced Systems*.
- Nonami et al., 2010 - Nonami, K., Kendoul, F., Suzuki, S., Wang, W., & Nakazawa, D., (2010). *Autonomous Flying Robots: Unmanned Aerial Vehicles and Micro Aerial Vehicles*, Springer.
- National Instruments™, (2003) LabVIEW™ *User Manual*, P.N.: 320999E-01, Ed., April, 2003.
- OSD, (2002). *UAV Roadmap 2002-2027*, Office of the Secretary of Defence (Acquisition, Technology, & Logistics), Air Warfare, December 2002.
- OSD, (2001). Office of the Secretary of Defence, *Unmanned Aerial Vehicles Roadmap*, April, 2001.
- OSD, (2005). Office of the Secretary of Defence, *Unmanned Aerial Systems Roadmap 2005-2030*, Technical Report.
- Ping Parallax, (2016) *Technical Datasheet*, (PING)), <https://www.parallax.com/product/28015>, Parallax Inc. [accessed June, 21, 2016].
- Picamera, (2013). <https://picamera.readthedocs.io/en/release-1.12/> . Release 1.12. [accessed July, 21, 2015].
- RC Logger, NovaX, (2015). *Operating Instructions*, RC EYE NovaX 350, <http://www.rclogger.com/support>, CEI Conrad Electronic International (HK) Limited.
- RC Logger, One Eye, (2015). *Operating Instructions*, RC EYE One Xtreme, <http://www.rclogger.com/support>, CEI Conrad Electronic International (HK) Limited.
- RaspberryPi camera (2016), <https://www.raspberrypi.org/products/camera-module/>, [accessed February, 16, 2016].
- RaspberryPi (2016), Technical Documentation, <https://www.raspberrypi.org/documentation/> . [accessed July, 5, 2016].
- Sobers et al., 2009 - Sobers, D.R. Jr., Chowdhary, D., & Johnson, E.N., (2009). Indoor Navigation for Unmanned Aerial Vehicles. *AIAA Guidance, Navigation, and Control Conference*, pp. 10-13.
- Sharp, (2006). GP2Y0A02YK0F infrared sensor, *Data Sheet*, Sheet No.: E4-A00101EN, ©SHARP Corporation.
- Song et al., 2004 - Song, K., Chen, C., & Chiu Huang, C., (2004). Design and Experimental Study of an Ultrasonic Sensor System for Lateral Collision Avoidance at Low Speed. *IEEE Intelligent Vehicles Symposium*, IEEE, pp. 647-652.
- Sharp et al., 2001 - Sharp, C.S., Shakeria, O., & Sastry, S.S., (2001). A vision System for Landing an Unmanned Aerial Vehicle. *IEEE International Conference on Robotics & Automation*, IEEE, Vol. 2, pp. 1720-1727.
- Timmins, H., (2011). Robot Integration Engineering a GPS module with the Arduino. *Practical Arduino Engineering*, Springer Science+ Business Media, New York, Chap. 5, pp. 97-131.
- Tardos et al., 1990 - Tardos, J.D., Neira, J., Newman, P.M., & Leonard, J.J., (1990). Robust mapping and localization in indoor environments using sonar data. *International Journal of Robotics Research*, vol. 21, no.6, pp. 560-569.

- US Army, (2010). *Roadmap for UAS 2010-2035*, US Army UAS Center of Excellence (ATZQ-CDI-C), Forth Rucker, Alabama.
- Valavanis, K.P., (2008). *Advances in Unmanned Aerial Vehicles – State of Art and the Road to Autonomy*, Springer Science & Business Media, Vol. 33.
- Valavanis et al., 2008a - Valavanis, K.P., & Kontitis, M., (2008). A historical perspective on unmanned aerial vehicles. *Advances in Unmanned Aerial Vehicles – State of Art and the Road to Autonomy*, Springer Science & Business Media, Vol. 33, pp. 15-48.
- Valavanis et al., 2008b - Valavanis, K.P., Vatchesevanos, & G.J., Anstaklis, (2008). Conclusion and the Road Ahead. *Advances in Unmanned Aerial Vehicles – State of Art and the Road to Autonomy*, Springer Science Business & Media, Vol. 33, pp. 533-543
- Wang et al., 2013 - Wang, Y., Le, S., Fan, Z., (2013). A New Type of Rotor + Airbag Hybrid Unmanned Aerial Vehicle, *International Journal of Energy Science (IJES)*, Vol. 3., no. 3, pp. 183-187.
- Yi et al., 2000 - Yi, Z., Khing, H.Y., Seng, C.C., Wei, Z.X., (2000). Multi-ultrasonic sensor fusion for mobile robots. *Proceedings of 2000 IEEE Int. Symposium on Intelligent Vehicle*, IEEE, pp. 602-607.